UNIVERSITY OF CALIFORNIA
Santa Barbara

Micro-macro modeling and computation of ferrofluids

A Dissertation submitted in partial satisfaction
of the requirements for the degree of

Doctor of Philosophy

in

Mathematics

by

Jon T. Lo Kim Lin

Committee in Charge:

Professor Hector D. Ceniceros, Chair

Professor Carlos J. García-Cervera

Professor Xu Yang

December 2016

The Dissertation of
Jon T. Lo Kim Lin is approved:

Professor Carlos J. García-Cervera

Professor Xu Yang

Professor Hector D. Ceniceros, Committee Chairperson

November 2016

Micro-macro modeling and computation of ferrofluids

by

Jon T. Lo Kim Lin

Acknowledgements

I would like to express the sincerest gratitude to my advisor Hector Ceniceros. This dissertation would not be possible without his counsel. In addition, I would like to thank my committee members, Professor García-Cervera and Professor Yang for conveying an enthusiasm in scholarly research, and a passion in regard to teaching. Lastly, a special thank you to Professor Ken Millet, his mentorship and outreach played an important role in getting me into graduate school.

Curriculum Vitæ

Jon T. Lo Kim Lin

Personal

Born October 4, 1986 Paramaribo, Suriname

Education

2010 Bachelor of Arts in Mathematics, University of California, Berkeley

2014 Master of Arts in Mathematics, University of California, Santa Barbara

2016 (Expected) Doctor of Philosophy in Mathematics, University of California, Santa Barbara

Technical Skills

Languages: Object-oriented Fortran, Python, C, MATLAB, and shell scripting.

Libraries: BLAS, LAPACK, FFTW, NumPy, Pandas, Matplotlib, SciPy, Seaborn

Tools: Secure Shell (SSH), IPython, Emacs, Make, git, Valgrind, Eclipse, LaTeX.

Operating Systems: Linux and macOS.

Publications

R.F. Brown and J. T. Lo Kim Lin. Coincidences of projections and linear n-valued maps of tori. *Topology and its Applications*, 157(12), pp.1990-1998, 2010.

Abstract

Micro-macro modeling and computation of ferrofluids

Jon T. Lo Kim Lin

We present an innovative, effective micro-macro numerical approach for modeling ferrofluids under the presence of a magnetic field and a driven-cavity flow. Our multi-model approach combines the localized use of a microscopic Smoluchowski equation solver and a continuous constitutive law coupled with the macroscopic flow and an externally applied magnetic field. The model is confirmed with a direct simulation and results are compared with the closure approximation proposed by Shen and Doi [41]. We systematically study the change in viscosity by incrementally changing the numerical parameter settings. Indeed, "negative change" in viscosity is observed.

Contents

List of Figures

List of Tables

Chapter 1

Introduction

Complex fluids, also known as non-Newtonian fluids, are binary mixtures that have a coexistence between two phases: solid-liquid (suspensions or solutions of macromolecules such as polymers), solid-gas (granular), liquid-gas (foams), or liquid-liquid (emulsions). These fluids are truly ubiquitous: food industry (mayonnaise, egg whites, jellies); materials industry (plastics or polymeric fluids); biology or medicine (blood, synovial liquid); civil engineering (fresh concrete, paints); environment (snow, muds, lava); cosmetics (shaving cream, toothpaste, nail polish); etc. Most of all, these fluids may manifest counter-intuitive behaviors, such as, for polymeric fluids, the open syphon effect, or the rod climbing effect (also called the Weissenberg effect).

This dissertation is centered around ferrofluids, a special solid-liquid class of complex fluids. Ferrofluids, a portmanteau of ferromagnetic and fluids, is an artificial

colloidal suspension consisting of ferromagnetic nanoparticles in a liquid, such as water or some other type of oily liquid. Here, nanoparticles are objects measured in nanometers, where a nanometer denotes one billionth of a meter in the metric system. Anything measured in nanometers is considered microscopic. The magnetic nanoparticles in a ferrofluid are generally less than 10 nanometers in diameter; compare this to the size of a water molecule at 0.278 nanometers.

Above all, ferrofluids possess a property called paramagnetism; a form of magnetism that occurs only in the presence of an externally applied magnetic field. In other words, the (microstructure) nano-sized magnetic particles in a ferrofluid only become magnetic when a naturally magnetic object comes into contact with them. In brief, the fluid's non-Newtonian behavior is ascribable to the presence of the aforementioned magnetic particles; the evolutions of which are strongly coupled to the solvent dynamics.

We are interested in cases where the microstructures are very numerous (per unit volume, say), the microstructures are small and light (prevents sedimenting), and the solvent (carrier-fluid) is Newtonian. From this point, we exploit local thermodynamic equilibrium assumptions to assert that the microscopic configurations reach a stationary state (given the macroscopic quantities) within a timescale of several orders of magnitudes smaller than the macroscopic timescale. Also, due to length scale separations, we also employ mean field approximations, in other words, replace

the many-particle system at the microscopic level by a one-particle problem within an averaged environment. Hence; macroscopic quantities are obtained as averages over microscopic quantities (locally at the macroscopic time and length scale).

Our micro-macro formulation couples the (macroscopic) Navier-Stokes equations with a (microscopic) Smoluchowski equations system. To that effect, we regard the ferrofluid as a dilute suspension of spherical Brownian particles with a constant magnetic moment in a Newtonian solvent. We further assume that the magnetic moment is fixed to the particle and neglect interparticle dipole interaction.

In the language of kinetic theory, the configuration of an individual rod can be described by the vector $\mathbf{u}$, where the set of all possible values for $\mathbf{u}$ is called the configuration space. Within each macroscopic fluid element, at position $\mathbf{x}$ in the flow domain,

$$\psi(\mathbf{u}, \mathbf{x}, t) d\,\mathbf{u}, \tag{1.1}$$

indicates the probability of finding a magnetic moment in the configuration between $\mathbf{u}$ and $\mathbf{u} + d\,\mathbf{u}$ at time t and position $\mathbf{u}$.

When our fluid is at rest, namely under equilibrium conditions when the flow velocity $\mathbf{v}$ vanishes identically, configurations obey the Gibbs distribution ψ_{eq} that results from a balance between Brownian and elastic forces. Consequently, the additional (non-Newtonian) magnetic stress is trivial.

On the contrary, under nonequilibrium conditions when the configuration is influenced by the flow velocity gradient, our distribution function no longer coincides with the equilibrium value $\psi_{eq}(\mathbf{u})$, and varies in both physical space and time, say $\psi = \psi(\mathbf{u}, \mathbf{x}, t)$. In this case, contributions to each macroscopic fluid element from microscopically induced magnetic stresses and magnetic torque are now of the utmost rheological importance.

The flow velocities and stresses are coupled through conservation principles which leads to a challenging nonlinear problem. Expressly, there is the diffusion or Smoluchowski equation [1] that governs the evolution of our probability distribution function ψ, and a phenomenological expression relating the additional magnetic stress to ψ, see: Doi and Edwards [29]. To date, three competing strategies proliferate multiscale modeling of non-Newtonian fluids. Namely, the continuum, Fokker-Planck, and stochastic approach, respectively. For a concise treatise, see Keunings [38].

This dissertation follows the Fokker-Planck approach, wherein we solve every governing equation directly, that is, in both configuration and physical spaces. The distribution function ψ is calculated explicitly as a solution of the Smoluchowski equation and the additional (non-Newtonian) magnetic stress involves a particular average computed with ψ over all possible configurations. The dimensionality of the problem

[1] In the literature, Fokker-Planck and Smoluchowski are often used interchangeably. However, Fokker-Planck is an equation in which both momentum and configurational coordinates are used, whereas in the Smoluchowski equation, momentum (velocity) fluctuations have decayed. Upshot, while both equations take the same general form, they describe dynamics at different time scales.

is formidable, and models with many configuration degrees of freedom are computationally intractable. This explains why relatively few studies in the literature solve the Smoluchowski equation directly.

Chapter 2

The model

2.1 Micro-macro model

In a bounded domain, say D, modeling incompressible fluids involves the mass and momentum conservation equations:

$$\rho\left(\frac{D\,\mathbf{v}}{Dt}\right) = -\nabla p + \operatorname{div}\,\mathbf{T}, \tag{2.1}$$

$$\operatorname{div}\,\mathbf{v} = 0, \tag{2.2}$$

furnished with suitable boundary and initial conditions. Here

$$\frac{D}{Dt} = \frac{\partial}{\partial t} + (\mathbf{v}\cdot\nabla)\,, \tag{2.3}$$

stands for the material derivative [1], $\mathbf{v}$ is the flow velocity, p is the pressure, ρ is the density, and $\mathbf{T}$ represents the (Cauchy) stress tensor.

For Newtonian fluids, we have a linear relationship betweens stress and the (deformation) strain rate, $\mathbf{D}$:

$$\mathbf{T} = \eta_0 \left(\nabla \mathbf{v} + \nabla \mathbf{v}^T \right) = 2\eta_0 \, \mathbf{D}, \tag{2.4}$$

with η_0 being the viscosity of our Newtonian solvent (carrier-fluid).

Meanwhile, in the case of (non-Newtonian) ferrofluids, an additional stress tensor stemming from the ferrofluid's microstructure is introduced in the constitutive relation

$$\mathbf{T} = \eta_0 \left(\nabla \mathbf{v} + \nabla \mathbf{v}^T \right) + \mathbf{T}_m \, . \tag{2.5}$$

Our tensor $\mathbf{T}_m$ encapsulates the coupling of the microstructure (the magnetic nano-particles) with the macroscopic flow.

An imposed external magnetic field, say $\mathbf{H}_{\mathrm{ext}}$, interacts with the magnetic particles to affect their magnetization which in turn influences our fluid's viscosity. The magnetic induction $\mathbf{B}$ and the stray field $\mathbf{H}_s$ of the system satisfies the magnetostatic Maxwell's equations [19].

[1] Here, ∇ denotes the covariant derivative of a vector.

$$\operatorname{div} \mathbf{B} = 0 \quad \text{in} \quad D, \tag{2.6}$$

$$\nabla \times \mathbf{H}_s = \mathbf{0} \quad \text{in} \quad D. \tag{2.7}$$

The magnetic field, magnetic induction, and magnetization are related by

$$\mathbf{B} = \mu_0 \left(\mathbf{H}_s + \mathbf{M} \right), \tag{2.8}$$

where μ_0 denotes the magnetic permeability of vacuum. To date, computations in the literature focus almost exclusively on the superparamagentic case in which $\mathbf{M}$ is collinear with $\mathbf{H}_s$ and the magnetic stress contribution reduces to

$$\mathbf{T}_m = \mu_0 \, \mathbf{H} \otimes \mathbf{H} - \tfrac{1}{2} H^2 \mathbf{I}. \tag{2.9}$$

In contrast, we model the behavior of rigid rod-like microstructures in the configuration space S^2, and obtain the stress $\mathbf{T}_m$ as a function of the configurations of these microstructures [29]. In short, we derive $\mathbf{T}_m = \mathbf{T}_m(\mathbf{h}, \psi)$ from a microscopic perspective as outlined in [41], [28] and arrive at the Smoluchowski equation[2]

$$\frac{\partial \psi}{\partial t} + \left(\mathbf{v} \cdot \nabla_{\mathbf{x}} \right) \psi = \frac{1}{2\tau_B} \boldsymbol{\mathcal{R}} \cdot \left[\boldsymbol{\mathcal{R}} \psi + \frac{\mu_0 m}{\kappa_B T} \left(\mathbf{H}_{eff} \times \mathbf{u} \right) \psi \right] - \boldsymbol{\mathcal{R}} \cdot \left(\boldsymbol{\Omega} \, \psi \right). \tag{2.10}$$

[2]We are in a situation of dilute suspensions, hence; one ignores both the hydrodynamic and magnetic interparticle (dipole) interactions.

Here, $\psi = \psi(\mathbf{x}, \mathbf{u}, t)$ denotes the probability of finding a magnetic moment, say $\mathbf{m} = m\,\mathbf{u}$, in the configuration $\mathbf{u} \in S^2$ at the spatial location $\mathbf{x} \in \mathbb{R}^3$ at time t. Furthermore, κ_B is the Boltzmann constant, T is the temperature,

$$\tau_B = \frac{3V\eta_0}{k_B T}, \tag{2.11}$$

denotes the Brownian rotational relaxation time (V being the volume of the particle),

$$\boldsymbol{\mathcal{R}} = \mathbf{u} \times \frac{\partial}{\partial\,\mathbf{u}}, \tag{2.12}$$

is the rotational gradient operator,

$$\mathbf{H}_{eff} = \mathbf{H}_s + \mathbf{H}_{ext}, \tag{2.13}$$

is the effective field, and

$$\boldsymbol{\Omega} = \tfrac{1}{2}\nabla \times \mathbf{v}, \tag{2.14}$$

is the (local) angular velocity of the fluid. Finally, the (macroscopic) magnetization,

$$\mathbf{M} = nmM_s\langle \mathbf{u} \rangle_\psi, \tag{2.15}$$

is an ensemble average of the microscopic magnetization $m\,\mathbf{u}$ times (the number of particles per unit volume) n, where M_s denotes the saturation magnetization ($\mathbf{M}\cdot\mathbf{M} = M_s^2$). Also, $\langle\mathbf{u}\rangle_\psi$ is the first moment of ψ :

$$\langle\mathbf{u}\rangle_\psi = \int_{S^2} \mathbf{u}\,\psi(\mathbf{x},\mathbf{u},t)\,d\,\mathbf{u}\,. \tag{2.16}$$

2.2 Dimensional analysis

Our governing equations consist of the incompressible Navier-Stokes equations coupled with Maxwell's equations, and the microscopic Smoluchowski equation via the (Cauchy) stress tensor $\mathbf{T}$. More specifically,

$$\rho\left(\frac{D\,\mathbf{v}}{Dt}\right) = -\nabla p + \text{div }\mathbf{T}, \tag{2.17}$$

$$\text{div }\mathbf{v} = 0, \tag{2.18}$$

where,

$$\mathbf{T} = 2\eta_0\,\mathbf{D} + \mathbf{T}_m, \tag{2.19}$$

with the deformation strain

$$\mathbf{D} = \tfrac{1}{2}\left(\nabla\,\mathbf{v} + \nabla\,\mathbf{v}^T\right), \tag{2.20}$$

and the additional (non-Newtonian) magnetic stress is obtained from the principle of virtual work [41], [29]:

$$\mathbf{T}_m = 5\Phi_0\eta_0\,\mathbf{D} - \tfrac{1}{2}\mu_0\left[\mathbf{H}_{\text{eff}} \otimes \mathbf{M} - \mathbf{M} \otimes \mathbf{H}_{\text{eff}}\right], \tag{2.21}$$

where $\Phi_0 = Vn$ is the volume fraction of the nano-sized magnetic particles in the ferrofluid, and $\otimes$ denotes the standard tensor product, respectively.

For the lid-driven cavity problem, the Navier-Stokes equations have two important parameters, namely, density, say ρ, and Newtonian viscosity, η_0. In addition, the boundary conditions have a size characterized by a length L_c and velocities characterized by a velocity V_c. The characteristic velocity V_c is a representative fluid velocity in the flow domain. The characteristic length L_c characterizes the lengths over which the velocities change by an amount proportional to V_c. At the same time, we impose no-slip boundary conditions which are independent in time, thus; four parameters define the steady Navier-Stokes problem. This leads to the following two dimensionless parameters. In non-dimensionalizing the equations, the structure of the Navier-Stokes equations leads to the definition of the Reynolds number and the (magnetic) Mason number.

We put dimensionless variables by starred properties, say $\mathbf{x} = L_c\mathbf{x}^*$, so

$$x^* = \frac{x}{L_c}, \quad y^* = \frac{y}{L_c}, \quad z^* = \frac{z}{L_c}, \tag{2.22}$$

and the corresponding spatial derivates as:

$$\nabla = \frac{1}{L_c}\nabla^*, \tag{2.23}$$

and

$$\Delta = \frac{1}{L_c^2}\Delta^*. \tag{2.24}$$

We normalize the velocity by the characteristic velocity V_c :

$$\mathbf{v} = V_c\,\mathbf{v}^*\,. \tag{2.25}$$

For the time, we choose a characteristic time[3] that describes the fastest process in the system. Since our flow is steady we use the characteristic flow time

$$T_c := L_c/V_c, \tag{2.26}$$

hence;

$$t = T_c t^* = \frac{L_c}{V_c}t^*, \tag{2.27}$$

[3]In this situation the Strouhal number $St = T_c V_c/L_c = 1$.

thus,

$$\frac{\partial}{\partial t} = \frac{1}{T_c}\frac{\partial}{\partial t^*} = \frac{V_c}{L_c}\frac{\partial}{\partial t^*}. \tag{2.28}$$

For the pressure, we non-dimensionalize as:

$$p = P_c p^*, \tag{2.29}$$

where P_c is still to be determined. From the equations

$$\rho\frac{D\,\mathbf{v}}{Dt} = -\nabla p + \nabla\cdot(2\eta_0\mathbf{D}) + \nabla\cdot\mathbf{T}_m, \tag{2.30}$$

$$= -\nabla p + \nabla\cdot(2\eta_0\,\mathbf{D}) + \nabla\cdot\left(5\Phi_0\eta_0\,\mathbf{D} - \frac{1}{2}\mu_0\left(\mathbf{H}_{\text{eff}}\otimes\mathbf{M} - \mathbf{M}\otimes\mathbf{H}_{\text{eff}}\right)\right), \tag{2.31}$$

$$= -\nabla p + \nabla\cdot(2\eta_0\,\mathbf{D}) + \nabla\cdot\left(5\Phi_0\eta_0\,\mathbf{D} - \frac{1}{2}n\lambda k_B T\left(\mathbf{h}\otimes\langle\langle\mathbf{u}\rangle_\psi - \langle\mathbf{u}\rangle_\psi\otimes\mathbf{h}\right)\right), \tag{2.32}$$

$$= -\nabla p + (2+5\Phi_0)\eta_0\nabla\cdot\mathbf{D} - \frac{1}{2}n\lambda k_B T\nabla\cdot\left(\mathbf{h}\otimes\langle\mathbf{u}\rangle_\psi - \langle\mathbf{u}\rangle_\psi\otimes\mathbf{h}\right), \tag{2.33}$$

we obtain:

$$\rho\frac{V_c^2}{L_c}\frac{D\,\mathbf{v}^*}{Dt^*} = -\frac{P_c}{L_c}\nabla^* p^* + (2+5\Phi_0)\eta_0\frac{V_c}{L_c^2}\nabla^*\cdot\mathbf{D}^* - \frac{n\lambda k_B T}{2L_c}\nabla^*\cdot\left(\mathbf{h}\otimes\langle\mathbf{u}\rangle_\psi - \langle\mathbf{u}\rangle_\psi\otimes\mathbf{h}\right). \tag{2.34}$$

By multiplying both sides of equation (2.34) by $Lc/\rho V_c^2$ we see that

$$\frac{D\,\mathbf{v}^*}{Dt^*} = -\frac{P_c}{\rho V_c^2}\nabla^* p^* + \frac{(2+5\Phi_0)\eta_0}{2\rho V_c L_c}\nabla^* \cdot (2\,\mathbf{D}^*) - \frac{n\lambda k_B T}{2\rho V_c^2}\nabla^* \cdot (\mathbf{h}\otimes\langle\mathbf{u}\rangle_\psi - \langle\mathbf{u}\rangle_\psi \otimes \mathbf{h})\,. \tag{2.35}$$

In the same fashion, we recast the Smoluchowski equation 2.10 as

$$\frac{\partial\psi}{\partial t} + (\mathbf{v}\cdot\nabla_{\mathbf{x}})\,\psi = \frac{1}{De}\boldsymbol{\mathcal{R}}\cdot[\boldsymbol{\mathcal{R}}\psi + \lambda\,(\mathbf{h}\times\mathbf{u})\,\psi] - \boldsymbol{\mathcal{R}}\cdot(\boldsymbol{\Omega}\,\psi)\,, \tag{2.36}$$

where De and λ are two very important dimensionless parameters. More specifically, De is called the Deborah number:

$$De = \frac{\frac{2\tau_B}{k_B T}}{\frac{L_c}{V_c}} = \frac{2\tau_B V_c}{k_B T L_c}, \tag{2.37}$$

it is the ratio of the orientational Brownian relaxation time scale of the (microscopic) rigid rods and the (macroscopic) time scale of the fluid, and λ, the strength of the magnetic field relative to thermal energy due to Brownian motion:

$$\lambda = \frac{\mu_0 m \| \mathbf{H}_{ext} \| M_s}{k_B T}. \tag{2.38}$$

Here, the effective field, $\mathbf{h}$, is non-dimensionalized with under the assumption that the stray field and the external applied magnetic field have comparable magnetic strength, in other words,

$$M_r = \frac{\|\mathbf{H}_s\|}{\|\mathbf{H}_{ext}\|} = 1. \tag{2.39}$$

Now, choosing $P_c = \rho V_c^2$, and omitting the starred decorations, we write the Navier-Stokes equations 2.17 in dimensionless form as:

$$\frac{D\,\mathbf{v}}{Dt} = -\nabla p + \frac{1}{Re}\nabla \cdot (2\mathbf{D}) - \frac{1}{M_C}\nabla \cdot (\mathbf{h} \otimes \langle \mathbf{u} \rangle_\psi - \langle \mathbf{u} \rangle_\psi \otimes \mathbf{h}), \tag{2.40}$$

$$\nabla \cdot \mathbf{v} = 0 \tag{2.41}$$

where Re denotes the Reynolds number,

$$Re = \frac{2\rho V_c L_c}{(2 + 5\Phi_0)\eta_0}, \tag{2.42}$$

and

$$M_C = \frac{2\rho V_c^2}{n\lambda k_B T}, \tag{2.43}$$

where the product $Re \cdot M_C$ is the (magnetic) Mason number.

The additional (non-Newtonian) magnetic stress, $\mathbf{T}_m$, takes the form:

$$\mathbf{T}_m = 5\Phi_0\eta_0\,\mathbf{D} - \frac{1}{2}n\lambda k_B T\left(\mathbf{h}\otimes\langle\mathbf{u}\rangle_\psi - \langle\mathbf{u}\rangle_\psi\otimes\mathbf{h}\right). \tag{2.44}$$

Lastly, a routine calculation using the incompressibly condition (2.41) makes it plain that

$$\nabla\cdot(2\,\mathbf{D}) = \Delta\,\mathbf{v}, \tag{2.45}$$

hence;

$$\frac{\partial\,\mathbf{v}}{\partial t} + (\mathbf{v}\cdot\nabla)\,\mathbf{v} = -\nabla p + \frac{1}{Re}\Delta\,\mathbf{v} - \frac{1}{M_C}\nabla\cdot\left(\mathbf{h}\otimes\langle\mathbf{u}\rangle_\psi - \langle\mathbf{u}\rangle_\psi\otimes\mathbf{h}\right), \tag{2.46}$$

$$\nabla\cdot\mathbf{v} = 0. \tag{2.47}$$

2.2.1 Computational challenges

The fully coupled micro-macro model involves a six-dimensional system whose mere size represents a daunting computational challenge. Indeed, we have macroscopic position $\mathbf{x}\in\mathbb{R}^3$, microscopic configuration $\mathbf{u}(\theta,\phi)\in S^2$, and time $t\in\mathbb{R}^+$. In a direct simulation, we are bound to solve the Smoluchowski equation at every single grid point of the physical space domain to advance the governing equations. This is a formidable task, and we cannot stress the computational complexity of this problem enough.

For instance, let N_p and N_c denote the number of grid (or collocation) points in physical space and configuration space, respectively. According to Swarztrauber [35], the spherical harmonic evaluations require at minimum 64-bit double precision floating-point representations to combat round-off error. Therefore, just to store gridded data (or spectral coefficients) of the Smoluchowski's probability density function (PDF) at a single time step, we require $N_p^3 \times N_c^2$ floating-point reals and the minimal cost of updating the PDF everywhere is $O(N_p^2 \times N_c^2)$. For this reason, a modest resolution of $N_p = 128$ and $N_c = 64$ leads to $N_p^2 \times N_c^3 = 2^{33}$, and given that a single double requires 8 bytes of storage, a single time-step update requires roughly 68.72 gigabytes of storage.

2.2.2 Closure approximation

We reduce the dimensionality of our problem by eliminating the troublesome configuration space altogether. Following Shen and Doi [41], we multiply both sides of the Smoluchowski equation (2.36) by $\mathbf{u}$, and after integrating by parts over the unit sphere S^2, we obtain the following system of ODE's in physical space

$$\frac{D}{Dt}\langle \mathbf{u} \rangle_\psi = -\frac{1}{\tau_B}\langle \mathbf{u} \rangle_\psi + \frac{\lambda}{2\tau_B}\Big(\mathbf{h} - \mathbf{h} \cdot \langle \mathbf{u} \otimes \mathbf{u} \rangle_\psi \Big) + \frac{1}{2}\Big(\nabla \mathbf{v} - \nabla \mathbf{v}^\top \Big) \cdot \mathbf{h} \,. \tag{2.48}$$

Although it is true that (2.48) is now completely free from any configuration space dependence, it now contains the second moments $\langle \mathbf{u} \otimes \mathbf{u} \rangle_\psi$, which are unknown. As a

matter of fact, if we continue with this integration approach and attempt to derive an expression for the second moment, it spawns an equation involving the third moments, and so forth. In other words, the set of equations 2.48 are not closed.

To lift the dependence on the second moment $\langle \mathbf{u} \otimes \mathbf{u} \rangle_\psi$, and obtain a closed equation, we use the following closure (decoupling) approximation:

$$\langle \mathbf{u} \otimes \mathbf{u} \rangle_\psi \approx A \langle \mathbf{u} \rangle_\psi \otimes \langle \mathbf{u} \rangle_\psi + B\mathbf{I}, \tag{2.49}$$

where A and B are chosen at ad hoc so that the approximation is exact at equilibrium. More specifically, if we let $L(\lambda)$ denote the Langevin function, say

$$L(\lambda) = \coth(\lambda) - \frac{1}{\lambda}, \tag{2.50}$$

then (2.49) is rigorously exact at equilibrium if we take

$$A = A(\lambda) = \left(\frac{1 - \dfrac{3L(\lambda)}{\lambda}}{L(\lambda)^2} \right) \tag{2.51}$$

and

$$B = B(\lambda) = \frac{L(\lambda)}{\lambda}. \tag{2.52}$$

In conclusion, if we define a (macroscopic) equilibrium magnetization, say

$$\mathbf{M}_0 = nmM_s L(\lambda)\,\mathbf{h}, \tag{2.53}$$

and the friction coefficient $\zeta = 2\tau_B n k_B T$, equation 2.48 is recast, in terms of the (macroscopic) magnetization $\mathbf{M}$, as

$$\frac{D\,\mathbf{M}}{Dt} = -\frac{1}{\tau_B}\left(\mathbf{M}-\mathbf{M}_0\right) + \frac{A(\lambda)}{\zeta}\left(\left(\mathbf{M}\times\mathbf{H}\right)\times\mathbf{M} + \left(\|\,\mathbf{M}_0\,\|^2 - \|\,\mathbf{M}\,\|^2\right)\mathbf{H}\right) + \boldsymbol{\Omega}\times\mathbf{M}\,. \tag{2.54}$$

Finally, the resulting ODE (2.54) is solved numerically using a 4th order Runge Kutta method [22]. For a complete derivation of the equations, see: [41]

Chapter 3

Numerical methods

3.1 Projection method

We implement the pressure-increment projection algorithm for the discretization of the Navier-Stokes equation. Our execution corresponds to PmII as presented in [10]. This leads to theoretical second order accuracy for both velocity and pressure under the proviso that all the spatial derivatives are second order accurate. Our spatial discretization is carried using the marker-and-cell (MAC) method akin to that found in Harlow and Welch [15]. The third-order Essentially Non-Oscillatory (ENO) upwind scheme is employed for the advective terms [7].

3.1.1 Pressure-increment projection algorithm

Given the flow velocity $\mathbf{v}^n$, and the pressure $p^{n-\frac{1}{2}}$, we advance the equations in three steps:

Step 1: Compute an intermediate field, say $\mathbf{v}^*$, by solving

$$\frac{\mathbf{v}^* - \mathbf{v}^n}{dt} = -\left(\mathbf{v}\cdot\nabla\,\mathbf{v}\right)^{n+\frac{1}{2}} - \nabla p^{n+\frac{1}{2}} + \frac{1}{Re}\Delta\,\mathbf{v}^{n+\frac{1}{2}} - \frac{1}{Ma}\,\mathrm{div}\;\mathbf{T}^n, \tag{3.1}$$

$$\mathbf{v}^*\Big|_{\partial D} = \mathbf{v}_{BC}^{n+1}, \tag{3.2}$$

Here, the advective term is extrapolated by way of the Adams-Bashforth formula,

$$\left(\mathbf{v}\cdot\nabla\,\mathbf{v}\right)^{n+\frac{1}{2}} = \frac{3}{2}\left(\mathbf{v}\cdot\nabla\,\mathbf{u}\right)^n - \frac{1}{2}\left(\mathbf{v}\cdot\nabla\,\mathbf{v}\right)^{n-1}. \tag{3.3}$$

Utilizing the standard five point central difference operator, say Δ_h, the diffusion term is treated implicitly as

$$\Delta\,\mathbf{v}^{n+\frac{1}{2}} = \frac{1}{2}\left(\Delta_h\,\mathbf{v}^* + \Delta_h\,\mathbf{v}^n\right), \tag{3.4}$$

and the pressure gradient as

$$\nabla p^{n+\frac{1}{2}} = \mathcal{G}p^{n-\frac{1}{2}}, \tag{3.5}$$

where

$$\mathcal{G}p_{i+\frac{1}{2},j} = \frac{p_{i+1,j} - p_{i,j}}{dx}, \tag{3.6}$$

$$\mathcal{G}p_{i,j+\frac{1}{2}} = \frac{p_{i,j+1} - p_{i,j}}{dy}. \tag{3.7}$$

Step 2: Compute a pressure update ϕ^{n+1} by solving the Poisson equation with homogeneous Von Neumann boundary conditions, that is,

$$\Delta\phi^{n+1} = \frac{\nabla \cdot \mathbf{v}^*}{\Delta t}, \tag{3.8}$$

$$\mathbf{n} \cdot \nabla\phi^{n+1}\Big|_{\partial D} = 0. \tag{3.9}$$

This is accomplished by solving

$$\Delta_h\phi^{n+1} = \frac{\mathcal{D}\,\mathbf{v}^*}{\Delta t}, \tag{3.10}$$

where

$$(\mathcal{D}\,\mathbf{v})_{i,j} = \frac{u_{i+1/2,j} - u_{i-1/2,j}}{\Delta x} + \frac{v_{i,j+1/2} - v_{i,j-1/2}}{\Delta y}. \tag{3.11}$$

Step 3: We update pressure and velocity according to

$$\mathbf{v}^{n+1} = \mathbf{v}^* - \Delta t \mathcal{G} \phi^{n+1}, \tag{3.12}$$

$$p^{n+1/2} = p^{n-1/2} + \phi^{n+1} - \frac{1}{2Re} (\mathcal{D}\, \mathbf{v}^*) . \tag{3.13}$$

In brief, the pressure-increment projection method involves solving two Helmholtz equations for $\mathbf{v}^* = (u^*, v^*)$ in (3.1) and one Poisson equation for ϕ^{n+1} in (3.10). To that end, we employ the object-oriented features in modern Fortran; see: Metcalf [31]. The derived data type `NavierStokesSolver` in [25] utilizes `PoissonSolver` and `HelmholtzSolver` from `modern_fishpack` [24], which in turn are thread safe modernizations of the cyclic reduction routines `genbun` and `poistg` in NCAR's `FISHPACK90` [17, 34].

3.1.2 Lid-driven cavity flow

To validate `NavierStokesSolver` we solve the two-dimensional lid-driven cavity flow. This benchmark problem has long history in testing new codes or new solution methods; its geometry is elementary and the boundary conditions are simple. Due to the problem's immense popularity, there is a wealth of well-established data to compare with. A good set of data for comparison is that of Ghia, Ghia, and Shin [44], since it includes tabular results for a wide range of Reynolds numbers.

Our Newtonian fluid is contained in a square domain $D = [0,1] \times [0,1]$ with Dirichlet boundary conditions on all sides, with three stationary sides and one moving side (with velocity tangent to the side). In our case, the top side of the unit-square cavity moves with speed 1.0 in the horizontal x-direction. The Reynolds number, based on the lid-speed, the cavity side-length, and the kinematic viscosity, is set to 100.

To investigate the spatial order of convergence, we compute the solution on five grids consecutively refined with a ratio of 2: 64×64, 128×128, 256×256, 512×512, and 1024×1024.

For each simulation, we have a uniform time step $\Delta t = \dfrac{\Delta x}{4}$ with total time $t = 30$. The tolerance for convergence is set at 10^{-12}.

We compute the observed order of convergence in space using the solution on three consecutive grids in the L^2-norm:

With flow velocity $\mathbf{v} = (u, v)$ and pressure p we obtain:

Table 3.1: The trio of grids employed to compute the observed order of convergence. The suffix (first, middle, or last) refers to the trio of grids used to compute the observed order.

first:	64×64, 128×128, and 256×256;
middle:	128×128, 256×256, and 512×512;
last:	256×256, 512×512, and 1024×1024.

Table 3.2: The observed order of convergence for the lid-driven cavity flow with $Re = 1.0$

u-first	u-middle	u-last
1.7695	2.116	1.9837

v-first	v-middle	v-last
1.5663	2.037	1.9341

p-first	p-middle	p-last
1.5703	1.9638	1.8206

3.2 Hybrid method: Maxwell's equations

We solve Maxwell's equations by modifying Fredkin and Koehler's hybrid method [11]. Equally important, our software is a modernization of earlier work by García-Cervera and Roma [5]. To summarize, the stray field can be written as

$$\mathbf{H}_s = \nabla\varphi, \tag{3.14}$$

where φ, the magnetostatic potential, solves the magnetostatic equation

$$\Delta\varphi = \operatorname{div}\mathbf{M} \quad \text{for} \quad \mathbf{x} \in D, \tag{3.15}$$

$$\Delta\varphi = 0 \quad \text{for} \quad \mathbf{x} \in \overline{D}^c, \tag{3.16}$$

$$[\varphi] = 0 \quad \text{for} \quad \mathbf{x} \in \partial D, \tag{3.17}$$

$$\left[\frac{\partial\varphi}{\partial\mathbf{n}}\right] = -\mathbf{M}\cdot\mathbf{n} \quad \text{for} \quad \mathbf{x} \in \partial D. \tag{3.18}$$

We decompose the magnetic static potential (3.14) as

$$\varphi = \varphi_1 + \varphi_2, \tag{3.19}$$

where φ_1 is chosen to satisfy the equation

$$\Delta\varphi_1 = \operatorname{div} \mathbf{M} \quad \text{for} \quad \mathbf{x} \in D, \tag{3.20}$$

$$\varphi_1 = 0 \quad \text{for} \quad \mathbf{x} \in \partial D, \tag{3.21}$$

and φ_1 is extended to be equal to zero outside D. The boundary contributions are included in φ_2, which satisfies the equation

$$\Delta\varphi_2 = 0 \quad \text{for} \quad \mathbf{x} \in D \cup \overline{D}^c, \tag{3.22}$$

$$[\varphi_2] = 0 \quad \text{for} \quad \mathbf{x} \in \partial D, \tag{3.23}$$

$$\left[\frac{\partial\varphi_2}{\partial\,\mathbf{n}}\right] = -\,\mathbf{M}\cdot\mathbf{n} + \frac{\partial\varphi_1}{\partial\,\mathbf{n}} \quad \text{for} \quad \mathbf{x} \in \partial D. \tag{3.24}$$

The solution to (3.22) is given by the double layer potential

$$\varphi_2(\mathbf{x}) = \int_{\mathbf{y}\,\in\,\partial D} \Gamma(\mathbf{x}-\mathbf{y}) g(\mathbf{y}) d\sigma(\mathbf{y}), \tag{3.25}$$

where Γ is the Newtonian potential in free space and

$$g(\mathbf{y}) = -\,\mathbf{M}\cdot\mathbf{n} + \frac{\partial\varphi_1}{\partial\,\mathbf{n}}. \tag{3.26}$$

The Neumann boundary values for φ_2 in (3.24) can be evaluated using the integral representation (3.25), and therefore φ_2 can be determined inside the domain solving a Poisson equation with Dirichlet boundary conditions. The integral (3.25)

is approximated on the boundary of the domain by approximating g using piecewise polynomial interpolation. The corresponding moments of the Newtonian potential can be evaluated analytically.

In the two-dimensional case, the resulting sum can be evaluated in $O(N)$ operation by direct summation, where N is the total number of grid points in the domain, if a uniform grid is used. In the 3-dimensional case, however, the evaluation of the boundary values by direct summation is an $O(N^{4/3})$ operation. Solving Poisson's equation with multigrid is an $O(N)$ operation. Therefore, in two dimensions this procedure has optimal complexity.

Our derived data type `MaxwellSolver` in [23] again employs `PoissonSolver` in `modern_fishpack` [24] to solve (3.20) and (3.22).

3.3 Spectral method

At each time step we wish to update ψ for every physical space point $\mathbf{x} \in D$ using 2.10. We need to proceed with caution to avoid the pole problem for finite difference schemes. More specifically, recall the Courant-Friedrichs-Lewy (CFL) condition [9] for the stability of explicit time-stepping algorithms:

$$\Delta t < \frac{\Delta x}{c}, \tag{3.27}$$

where c is the speed of the fastest waves allowed by the differential equation of interest and Δx is the smallest spatial grid interval. Using (co)latitude $(0 \leq \theta \leq \pi)$ and longitude $(0 \leq \phi \leq 2\pi)$ as coordinates, if we naively apply an uniform spacing in ϕ and θ, it follows from the circular arc formula that the distance, say Δx, between two grid points on a circle of colatitude θ is

$$\Delta x = \sin\theta \Delta\phi, \tag{3.28}$$

which tends to zero at the poles as shown graphically in the figure below.

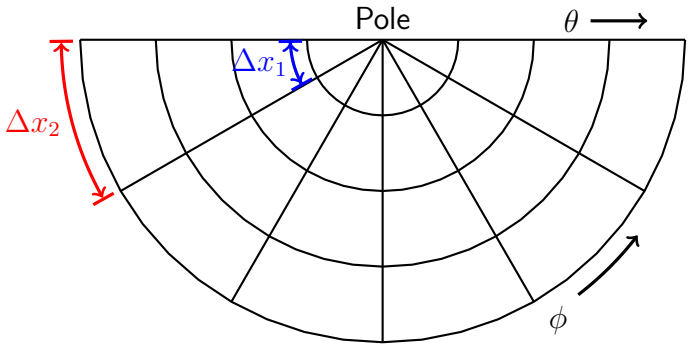

Figure 3.1: A grid with uniform spacing in latitude and longitude as viewed from Polaris, the Pole Star. The meridians (lines of constant longitude) all converge at the pole. consequently, $\Delta x \to 0$ as the pole is approached, even though $\Delta\phi$ is constant. The very small grid spacing near the pole is the "pole problem": One must use a prohibitively small time step, or the numerical flow will violate the Courant-Friedrichs-Levy criterion and become unstable.

We attack the root of the problem and solve for ψ using a series expansion method; employing the spherical harmonics (the angular portion of an orthogonal family of solutions to the surface Laplacian) as a basis set. Because of the natural connection between the spherical harmonics and the geometry of the sphere, the spherical harmonics provide equiareal resolution [1] (as a result of triangular truncation and the Addition Theorem, see [32]), exponential convergence, and a trivial inversion of the surface Laplacian, which is the eigen-operator for these functions.

3.3.1 Spherical harmonics

In $\mathbb{R}^3$, the Laplacian is given by

$$\Delta = \frac{\partial^2}{\partial x^2} + \frac{\partial^2}{\partial y^2} + \frac{\partial^2}{\partial z^2}. \tag{3.29}$$

In spherical coordinates $\{(r, \theta, \phi) \colon r \in \mathbb{R}^{\geq 0}, \theta \in [0, \pi], \phi \in [0, 2\pi)\}$, that is,

$$x = r \sin\theta \cos\phi, \tag{3.30}$$

$$y = r \sin\theta \sin\phi, \tag{3.31}$$

$$z = r \cos\theta, \tag{3.32}$$

[1] A numerical algorithm which has the property that its numerical characteristics are invariant to a rotation of the north pole of the coordinate system so that features of a given size are resolved equally well or badly regardless of whether they are located at the poles, equator, or anywhere in between.

the Laplacian takes the form

$$\Delta = \csc^2\theta \frac{\partial^2}{\partial\phi^2} + \frac{\partial^2}{\partial\theta^2} + \cot\theta\frac{\partial}{\partial\theta} + 2r\frac{\partial}{\partial r} + r^2\frac{\partial^2}{\partial r^2}. \tag{3.33}$$

Suppose that we have a homogeneous harmonic polynomial of degrees n, say

$$p_n(x, y, z) = r^n q_n(\theta, \phi). \tag{3.34}$$

Then

$$0 = \Delta p_n \tag{3.35}$$

$$= \left[\csc^2\theta\frac{\partial}{\partial\phi^2} + \frac{\partial^2}{\partial\theta^2} + \cot\theta\frac{\partial}{\partial\theta}\right] r^n q_n(\theta,\phi) + 2rnr^{n-1}q_n(\theta,\phi) + r^2 n(n-1)r^{n-2}q_n(\theta,\phi). \tag{3.36}$$

On S^2, we define the Laplace-Beltrami operator $\boldsymbol{\mathcal{R}}^2 := \Delta_S$ (surface Laplacian) by

$$\Delta_S = \csc\theta\frac{\partial^2}{\partial\phi^2} + \frac{\partial^2}{\partial\theta^2} + \cot\theta\frac{\partial}{\partial\theta}, \tag{3.37}$$

and see that

$$\Delta_S q_n(\theta,\phi) = -n(n+1)q_n(\theta,\phi). \tag{3.38}$$

This q_n is therefore an eigenfunction of the spherical Laplacian. Any such eigenfunction is called a spherical harmonic.

Indeed, the operator Δ_S is self-adjoint, which implies that the eigenspaces Λ_n are orthogonal. Λ_n consists of the homogeneous harmonic polynomials of degree n restricted to the sphere, and has dimension $2n+1$. On the sphere, the homogeneous harmonic polynomials span the set of all polynomials, which in turn are dense in L^2. Our spherical harmonics therefore span L^2. If we take a basis within each eigenspace then this collection will give a basis for L^2 of the sphere.

Upshot, any square-integrable function on S^2 can be approximated up to machine precision as a truncated sum of spherical harmonics. For a rigorous proof see Folland [14].

Spherical harmonics arise in $\mathbb{R}^3$ in the same fashion Fourier series arise in $\mathbb{R}^2$. That is, for fixed n, we can organize the Λ_n as

$$\left\{Y_n^m(\theta,\phi) = \tilde{P}_n^m(\cos\theta)e^{im\phi}/\sqrt{2\pi}\right\}_{-n\leq m\leq n}. \tag{3.39}$$

It is not immediately obvious that we can separate variables and assume exponential functions in the longitudinal (ϕ) directions. This follows from the fact that the lines of fixed θ are circles. For a rigorous construction see Boyd [3], or for a more gentle introduction see Strauss [43]. A disadvantage of this organization is that it makes the

poles into special points. We would like to find conditions on $\tilde{P}_n^m$ to make 3.39 into a set of smooth spherical harmonics. More specifically, we need to have

$$\Delta_S \frac{e^{im\phi}}{\sqrt{2\pi}} \tilde{P}_n^m(\cos\theta) = \left[\frac{\partial^2}{\partial\theta^2} + \cot\theta \frac{\partial}{\partial\theta} - \frac{m^2}{\sin^2\theta} \right] \frac{e^{im\phi}}{\sqrt{2\pi}} = -n(n+1) \frac{e^{im\phi}}{\sqrt{2\pi}} \tilde{P}_n^m(\cos\theta), \tag{3.40}$$

or equivalently,

$$\boldsymbol{\mathcal{R}}^2 Y_n^m(\theta,\phi) = -n(n+1) Y_n^m(\theta,\phi). \tag{3.41}$$

The relation 3.41 and the condition that $\tilde{P}_n^m(1) \neq \pm\infty$, identifies the $\tilde{P}_n^m$'s up to a constant as the Associated Legendre functions (of the 1st kind) of order m and degree n. We use the tilde to indicate the L^2 normalized version of the classically defined Associated Legendre functions, denoted P_n^m. Also, note that for each fixed m, the set $\{\tilde{P}_n^m(\cos\theta)\}_{n\geq|m|}$ will need to be orthogonal with respect to the measure $\sin\theta\, d\theta$, so that the harmonics from different Λ_n will be orthogonal.

3.3.2 Series expansion method

Generally speaking, the series expansion method involves a partial differential equation (PDE) with an operator H involving only derivatives in physical space, say

$$\frac{\partial f}{\partial t} + H(f) = 0, \tag{3.42}$$

to be solve on the spatial domain D subject to specified initial and boundary conditions. We write the spatial dependence of f as a linear combination of known expansion functions $\phi_i(\mathbf{x})$

$$f(\mathbf{x}, t) = \sum_{i \in \mathbb{N}} a_i(t)\phi_i(\mathbf{x}), \tag{3.43}$$

where $\{\phi_i\}_{i \in \mathbb{N}}$ span the Hilbert space L^2 with the standard inner product

$$\langle \phi, \varphi \rangle = \int_D \phi^* \varphi d\,\mathbf{x} \tag{3.44}$$

We truncate

$$\widetilde{f}(\mathbf{x}, t) = \sum_{i=1}^{N} a_i(t)\phi_i(\mathbf{x}), \tag{3.45}$$

where $\widetilde{f}$ approximates f. Our original PDE is now reduced to finding the unknown coefficients

$$a_1(t), a_2(t), \ldots, a_N(t) \tag{3.46}$$

in a way that minimized the error in the approximate solution. Now,

$$\frac{\partial f}{\partial t} + H(f) = 0 \quad \Longleftrightarrow \quad \frac{\partial \widetilde{f}}{\partial t} + H(\widetilde{f}) = R(\widetilde{f}), \tag{3.47}$$

where R quantifies how much $\widetilde{f}$ fails to satisfy the governing equation. Strategies for minimizing the residual R are:

1. Minimize the ℓ_2-norm of R: compute the $a_i(t)$ such as to minimize

$$\|R(\widetilde{f})\|_2 := \langle R(\widetilde{f}), R(\widetilde{f})\rangle^{1/2} = \left(\int_D R(\widetilde{f})R(\widetilde{f})\,dx\right)^{1/2} \tag{3.48}$$

2. Collocation method: constrain the residual by requiring it to be zero at a discrete set of grid points

$$R(\widetilde{f}) = 0 \quad \text{for all} \quad i = 1, 2, \ldots, N \tag{3.49}$$

3. Galerkin approximation: require R to be orthogonal to each of the expansion functions used in the expansion of f, i.e. the residual depends only on the omitted basis functions.

$$\langle \phi_i, R(\widetilde{f})\rangle = \int_D \phi_i^* R(\widetilde{f})\,dx = 0 \quad \text{for all} \quad i = 1, 2, \ldots, N \tag{3.50}$$

Each of these strategies ensues a N-system of coupled ordinary differential equations (ODE) for the time-dependent coefficients $a_i(t), i = 1, 2, \ldots, N$. In our case, Galerkin method and ℓ_2-norm minimization are equivalent [12]. Different series expansion methods use one or more of these strategies to minimize the error

- Collocation strategy is used in the pseudo-spectral method.
- Galerkin and ℓ^2-norm minimization are the basis of the spectral method.
- Galerkin approximation is used in the Finite-Element Method (FEM).

Given

$$\frac{\partial \widetilde{f}}{\partial t} + H(\widetilde{f}) = R(\widetilde{f}) \quad \text{and} \quad \widetilde{f} = \sum_{i=1}^{N} a_i \phi_i, \tag{3.51}$$

taking the inner product with all the expansion function and applying the Galerkin approximation:

$$\langle \phi_j, \frac{\partial \widetilde{f}}{\partial t} \rangle + \langle \phi_j, H(\widetilde{f}) \rangle - \cancel{\langle \phi_j, R(\widetilde{f}) \rangle} = 0 \quad \text{for all} \quad j = 1, 2, \ldots N, \tag{3.52}$$

$$\Rightarrow \quad \sum_{i=1}^{N} \left(\int_D \phi_j^* \phi_i \, dx \right) \frac{da_i}{dt} + \int_D \phi_j^* H \left(\sum_{i=1}^{N} a_i \phi_i \right) dx = 0 \tag{3.53}$$

for all $j = 1, 2, \ldots N$ with initial condition

$$\sum_{i=1}^{N} \left(\int_D \phi_j^* \phi_i \, dx \right) a_i(0) = \int_D \phi_j(x) f_0(x) \, dx. \tag{3.54}$$

Since our expansion functions have to satisfy the required boundary conditions, our approximated solution also satisfies these boundary conditions.

At first sight, these equations look more complicated than in Finite-Difference discretization. However, if we know the eigenfunctions e_i of H, i.e.,

$$H(e_i) = \lambda_i e_i, \tag{3.55}$$

then we reduce the problem to solving

$$\sum_{i=1}^{N} \left[\left(\int_D e_j^* e_i \, dx \right) \left(\frac{da_i}{dt} + \lambda_i a_i \right) \right] = 0 \quad \text{for all} \quad j = 1, 2, \ldots, N. \tag{3.56}$$

If the expansion functions e_i are orthogonal and normalized, then

$$\sum_{i=1}^{N} \left[\left(\int_D e_j^* e_i \, dx \right) \left(\frac{da_i}{dt} + \lambda_i a_i \right) \right] = 0 \quad \Rightarrow \boxed{\frac{da_i}{dt} + \lambda_i a_i = 0} \tag{3.57}$$

for all $j = 1, 2, \ldots, N$. We now have a decoupled system of ODE's which can be solved analytically. This is the spectral method.

To obtain a system of partial differential equations (PDE) for the spherical harmonics coefficients we multiply the Smoluchowski equations by Y_n^{m*} and integrate over the configuration space S^2. Since the harmonics are an orthonormal basis for S^2 and the eigenfunctions of $\boldsymbol{\mathcal{R}}^2$ it follows that 2.36 takes the form

$$\frac{\partial \psi_n^m}{\partial t} + (\mathbf{v} \cdot \nabla_{\mathbf{x}}) \, \psi_n^m = \frac{1}{De} \left(-n(n+1)\psi_n^m + \lambda P \left[\psi_n^m \right] \right) - A \left[\psi_n^m \right], \tag{3.58}$$

where

$$A\left[\psi_n^m\right] = \int_{S^2} \left(Y_n^m\right)^* \boldsymbol{\mathcal{R}} \cdot \left(\boldsymbol{\Omega}\, \psi\right)\, dS, \tag{3.59}$$

$$P\left[\psi_n^m\right] = \int_{S^2} \left(Y_n^m\right)^* \boldsymbol{\mathcal{R}} \cdot \left(\psi\, \left(\mathbf{h} \times \mathbf{u}\right)\right)\, dS, \tag{3.60}$$

and $[\psi_n^m]$ denotes the complete set of spectral coefficients of degree n and order m. To evaluate 3.59 and 3.60 we need to determine the effect of $\boldsymbol{\mathcal{R}}$ on each Y_n^m. Via the closely related angular momentum operator, $-i\boldsymbol{\mathcal{R}}$, where $i = \sqrt{-1}$, we find that

$$A\left[\psi_n^m\right] = \frac{1}{2} i \left(a_n^m \Omega^- (-1)^{m+1} Y_n^{m+1} + b_n^{m-1} \Omega^+ (-1)^{m-1} Y_n^{m-1}\right) + i\Omega_z m Y_n^m, \tag{3.61}$$

where $\Omega^{\pm} = \Omega_x \pm i\Omega_y$ for $\boldsymbol{\Omega} = (\Omega_x, \Omega_y, \Omega_z)$, and

$$a_n^m = \sqrt{n(n+1) - m(m+1)}, \tag{3.62}$$

$$b_n^m = \sqrt{n(n+1) - m(m-1)}. \tag{3.63}$$

Furthermore, using the relation

$$\boldsymbol{\mathcal{R}} Y_n^m \cdot \left(\mathbf{h} \times \mathbf{u}\right) = \mathbf{u} \cdot \left(\boldsymbol{\mathcal{R}} Y_n^m \times \mathbf{h}\right), \tag{3.64}$$

along with the familiar recurrence relations for the associated Legendre Functions, we obtain:

$$
\begin{aligned}
P\left[\psi_n^m\right] = & \frac{1}{2}H_z\left(a_{n+1}^m(-1)^{m+1}c_{n+1}^{-(m+1)} + b_{n+1}^m(-1)^{m-1}c_{n+1}^{m-1} + 2h_{n+1}^m\right)\psi_{n+1}^m \\
& - \frac{1}{2}H_z\left(a_{n-1}^m(-1)^{m+1}d_{n-1}^{-(m+1)} + b_{n-1}^m(-1)^{m-1}d_{n-1}^{m-1} + 2h_n^m\right)\psi_{n-1}^m \\
& + \left(H^-\left[(m+1)c_{n+1}^{-(m+1)} + d_{n-1}^{m-1}\right] - \frac{1}{2}H^+b_{n+1}^{m+1}(-1)^m h_{n+1}^m\right)\psi_{n+1}^{m+1} \\
& - \left(H^-\left((m+1)d_{n-1}^{-(m+1)} - c_{n+1}^{m-1}\right) + \frac{1}{2}H^+b_{n-1}^{m+1}(-1)^m h_n^m\right)\psi_{n-1}^{m+1} \\
& + \left(H^+\left[(m-1)c_{n+1}^{m-1} - d_{n-1}^{-(m+1)}\right] - \frac{1}{2}H^-a_{n+1}^{m-1}(-1)^m h_{n+1}^m\right)\psi_{n+1}^{m-1} \\
& - \left(H^+\left[(m-1)d_{n-1}^{m-1} + c_{n+1}^{-(m+1)}\right] + \frac{1}{2}H^-a_{n-1}^{m-1}(-1)^m h_n^m\right)\psi_{n-1}^{m-1}, \quad (3.65)
\end{aligned}
$$

where

$$
h_n^m = \sqrt{\frac{(n-m)(n+m)}{(2n+1)(2n-1)}}, \quad (3.66)
$$

$$
c_n^m = \sqrt{\frac{(n-m-1)(n-m)}{(2n-1)(2n+1)}} \quad (3.67)
$$

$$
d_n^m = \sqrt{\frac{(n+m+1)(n+m+2)}{(2n+1)(2n+3)}}, \quad (3.68)
$$

and $H^{\pm} = H_x \pm iH_y$ for $\mathbf{h} = (H_x, H_y, H_z)$.

To discretize 3.58 we use a semi-implicit first-order Euler's method. Notice that the Laplace-Beltrami term is treated implicitly. Lastly, because there are sharp gradients in the solution of the Smoluchowski equation, a third-order Essentially Non-Oscillatory (ENO) upwind scheme is implemented to calculate the physical space gradient term $(\mathbf{v}\cdot\nabla_{\mathbf{x}})\,\psi_n^m$.

Chapter 4

Results

We now discuss the numerical results obtained from implementing the fully coupled two-dimensional system and compare the rheological properties with that of the closure approximation.

To review, we solve the two-dimensional Navier-Stokes equations for the lid-driven cavity problem in a square domain[1], say $D = [0,1] \times [0,1]$, with Dirichlet boundary conditions on all sides, with three stationary sides and one moving side (with velocity tangent to the side).

[1]Please note that are no dimension incompatibility issues between the two-dimensional macro-structure (physical space) and the three-dimensional micro-structure (configuration space). Our model is in fact fully three-dimensional in that our microscopic particles are fully mobile, that is, we allow them to rotate out of the plane. Furthermore, all three components of the flow velocity $\mathbf{v}$ are nonzero and all components of stress tensor $\mathbf{T}_m$ and the (local) angular velocity $\boldsymbol{\Omega}$ are kept, yet we do not allow for gradients in the z-direction.

Exercising the International System of Units (SI), the scale parameters are $L_c = 10^{-3}\mathtt{m}$, $V_c = 10^{-1}\mathtt{m/s}$, $\rho = 10^{3}\mathtt{kg/m^3}$, $\eta_0 = 10^{-3}\mathtt{kg/(ms)}$ and $\Phi_0 = 3\%$. The Reynolds number, based on the lid-speed, the cavity side-length, and the kinematic viscosity, is set to 1. For the sake of investigation, we assume that $Ma = 1$. Considering ferrimagnetic (not to be confused with ferromagnetic) material containing Iron(II,III) oxide (Fe_3O_4), subject to a magnetic field at room temperature $T = 293\mathtt{K}$, with particle diameter $8\mathtt{nm}$, we have $\lambda \sim O(1)$.

At each time step, we solve the Smoluchowski equation in spectral space and extract the first moment from the coefficients via the relations

$$\mathbf{M}\cdot\mathbf{e}_1 = \frac{2\pi}{\sqrt{3}}\left(\psi_1^1 - \psi_1^{-1}\right), \tag{4.1}$$

$$\mathbf{M}\cdot\mathbf{e}_2 = \frac{2\pi}{\sqrt{3}}\left(\psi_1^{-1} + \psi_1^1\right), \tag{4.2}$$

$$\mathbf{M}\cdot\mathbf{e}_3 = \frac{2\sqrt{2}\pi}{\sqrt{3}}\left(\psi_1^0\right), \tag{4.3}$$

where $\{\mathbf{e}_1, \mathbf{e}_2, \mathbf{e}_3\}$ denotes the standard Euclidean basis for $\mathbb{R}^3$. The first moment is then used to solve Maxwell's equations from which we update the effective field. The Deborah number is kept in the range $0.125 \leq De \leq 2$. The external magnetic field is kept constant at $\mathbf{H}_{\text{ext}} = (0, 1, 0)$.

Let Δx denote the (uniform) discretization mesh size in physical space. For each simulation, we have a uniform time step $\Delta t = \frac{\Delta x}{8}$ with total time $t = 30$. The tolerance for convergence of the governing equations' residual is set at 10^{-12}.

4.1 Vorticity and stream lines

At steady state, the flow velocity's flooded vorticity and stream lines are presented in Figure 4.1. As expected, we see the formation of a large primary vortex in the center of our domain [13, 44].

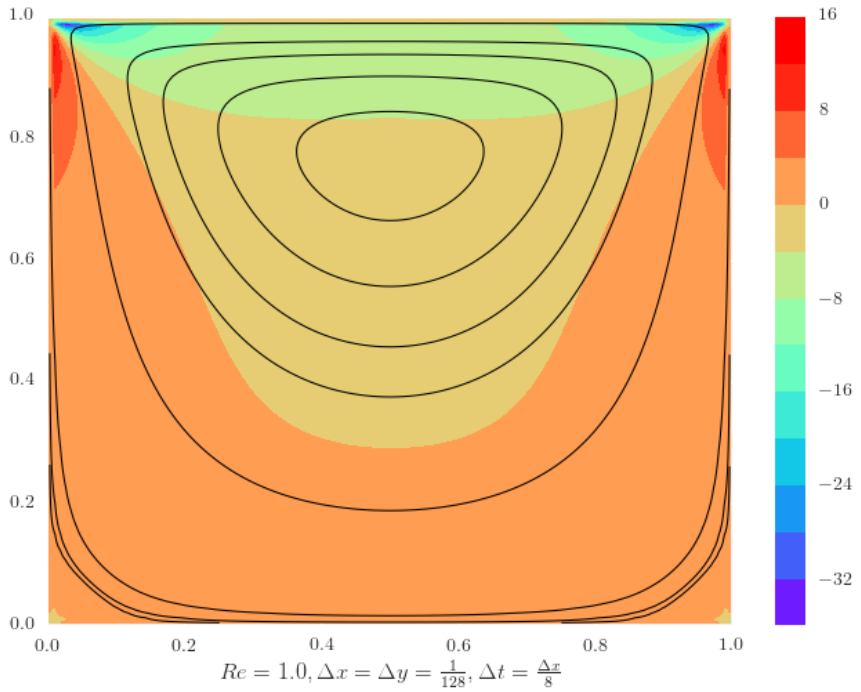

Figure 4.1: Flooded vorticity and superimposed stream lines for the lid-driven cavity flow of a Newtonian fluid for Reynolds number $Re = 1$ at steady state. Our contour fill color map extends outside the range of contour levels; data below the lowest contour level is violet, and above the highest level is red [16].

On the other hand, in the case our fully coupled system with magnetic stress and torque contributions, secondary vortices appear in the bottom corners of our domain. The secondary vortices are an interesting development as they are generally associated with Reynolds numbers of several orders of magnitude larger that our $Re = 1$, see: Ghia, Ghia, and Shin [44].

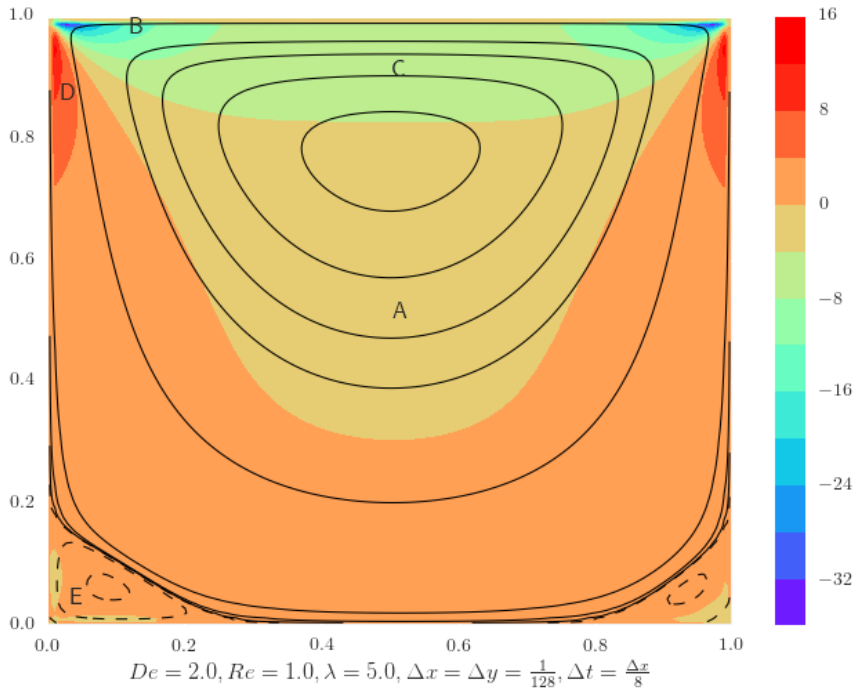

Figure 4.2: Flooded vorticity and superimposed stream lines for the lid-driven cavity flow of the (non-Newtonian) ferrofluid with significant magnetic stress and torque contributions. The important numerical parameters are the Reynolds number $Re = 1$, the Deborah number $De = 2$, and the strength of the magnetic field relative to thermal energy due to Brownian motion $\lambda = 5$. Our contour fill color map extends outside the range of contour levels; data below the lowest contour level is violet, and above the highest level is red [16]. Moreover, the labels A, B, C, D, and E, respectively, indicate the physical space locations where the vorticity exhibits sharp transitions from positive to negative values. That is, $A = (0.50390625, 0.50390625)$, $B = (0.12109375, 0.97265625)$, $C = (0.50390625, 0.90234375)$, $D = (0.01953125, 0.86328125)$. and $E = (0.03515625, 0.03515625)$.

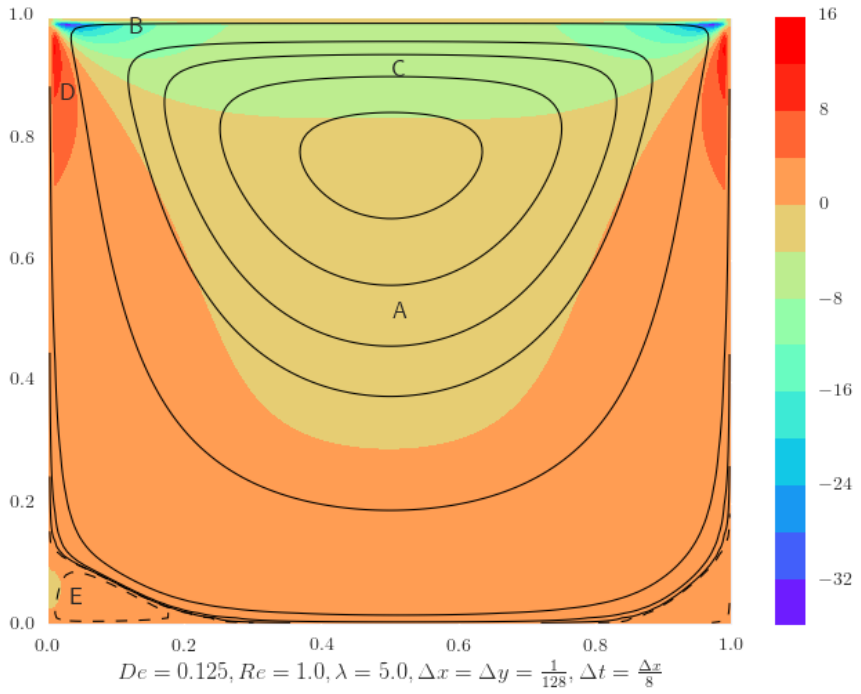

Figure 4.3: Flooded vorticity and superimposed stream lines for the lid-driven cavity flow of the (non-Newtonian) ferrofluid with moderate magnetic stress and torque contributions. The important numerical parameters are the Reynolds number $Re = 1$, the Deborah number $De = 0.125$, and the strength of the magnetic field relative to thermal energy due to Brownian motion $\lambda = 5$. Our contour fill color map extends outside the range of contour levels; data below the lowest contour level is violet, and above the highest level is red [16]. Moreover, the labels A, B, C, D, and E, respectively, indicate the physical space locations where the vorticity exhibits sharp transitions from positive to negative values. That is, $A = (0.50390625, 0.50390625)$, $B = (0.12109375, 0.97265625)$, $C = (0.50390625, 0.90234375)$, $D = (0.01953125, 0.86328125)$. and $E = (0.03515625, 0.03515625)$.

4.2 The stray field

Since the stray field varies in our domain, the magnetic stress also depends on the positions in our (physical space) domain, hence; the viscosity in our domain varies. Below we visualize the horizontal (x-direction) and vertical (y-direction) components of the stray field as we incrementally increase our dimensionless magnetic parameter $0.5 \leq \lambda \leq 7.5$.

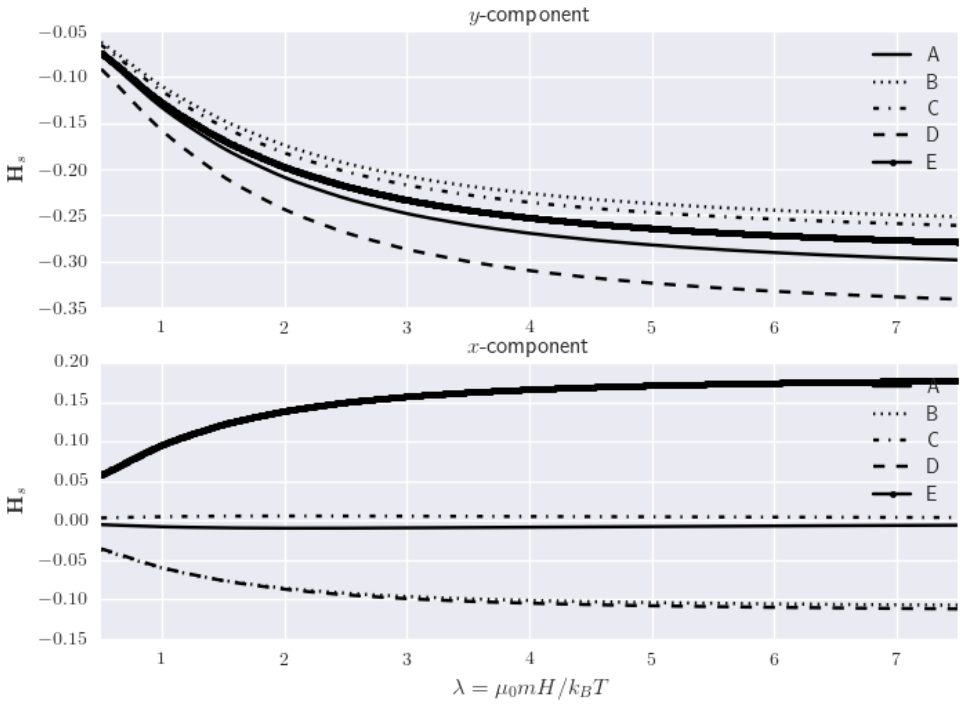

Figure 4.4: Plot of the (horizontal) x-component and (vertical) y-component of the stray field, say $\mathbf{H}_s \cdot \mathbf{e}_i$, versus the dimensionless magnetic parameter (the strength of the magnetic field relative to thermal energy due to Brownian motion), say λ, for the closure approximation. Here $\mathbf{e}_i$ denotes the standard Euclidean basis element in $\mathbb{R}^3$. The important (fixed) numerical parameters are the Reynolds number $Re = 1$ and the Deborah number $De = 0.125$. Moreover, the labels A, B, C, D, and E, respectively, indicate the physical space locations where the vorticity exhibits sharp transitions from positive to negative values in Figure 4.2. More specifically, $A = (0.50390625, 0.50390625)$, $B = (0.12109375, 0.97265625)$, $C = (0.50390625, 0.90234375)$, $D = (0.01953125, 0.86328125)$. and $E = (0.03515625, 0.03515625)$.

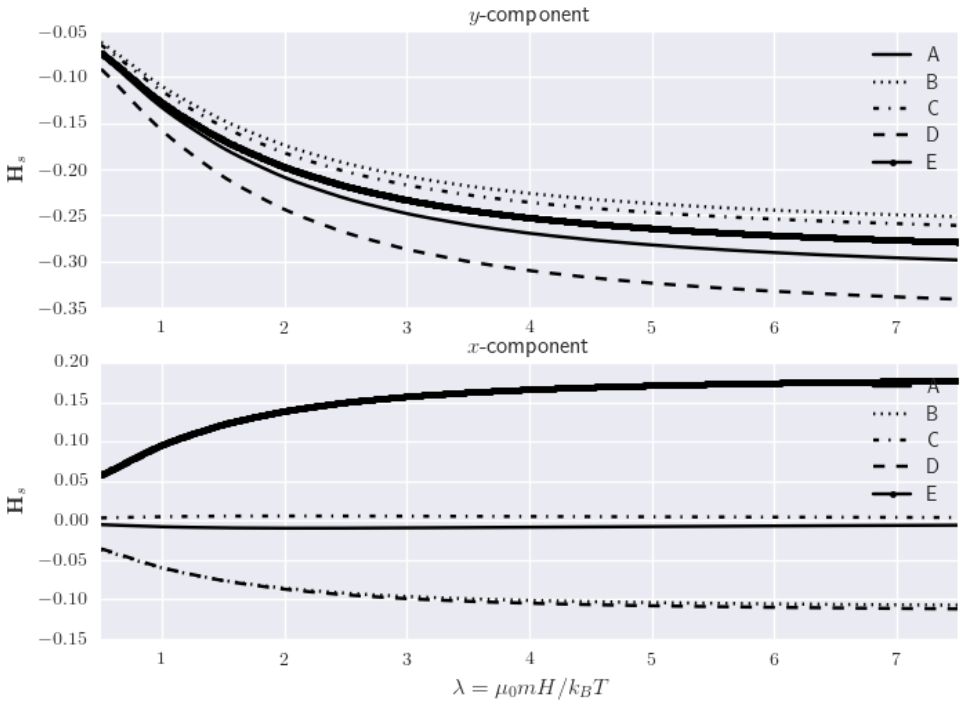

Figure 4.5: Plot of the (horizontal) x-component and (vertical) y-component of the stray field, say $\mathbf{H}_s \cdot \mathbf{e}_i$, versus the dimensionless magnetic parameter (the strength of the magnetic field relative to thermal energy due to Brownian motion), say λ, for the fully coupled system. Here $\mathbf{e}_i$ denotes the standard Euclidean basis element in $\mathbb{R}^3$. The important (fixed) numerical parameters are the Reynolds number $Re = 1$ and the Deborah number $De = 0.125$. Moreover, the labels A, B, C, and D, respectively, indicate the physical space locations where the vorticity exhibits sharp transitions from positive to negative values in Figure 4.2. More specifically, $A = (0.50390625, 0.50390625)$, $B = (0.12109375, 0.97265625)$, $C = (0.50390625, 0.90234375)$, and $D = (0.01953125, 0.86328125)$.

Since $De < 1$, the additional (non-Newtonian) magnetic stress and torque contributions are relatively moderate, and the general trend in the closure approximation's plot agrees with our fully coupled system in the case of weak flow.

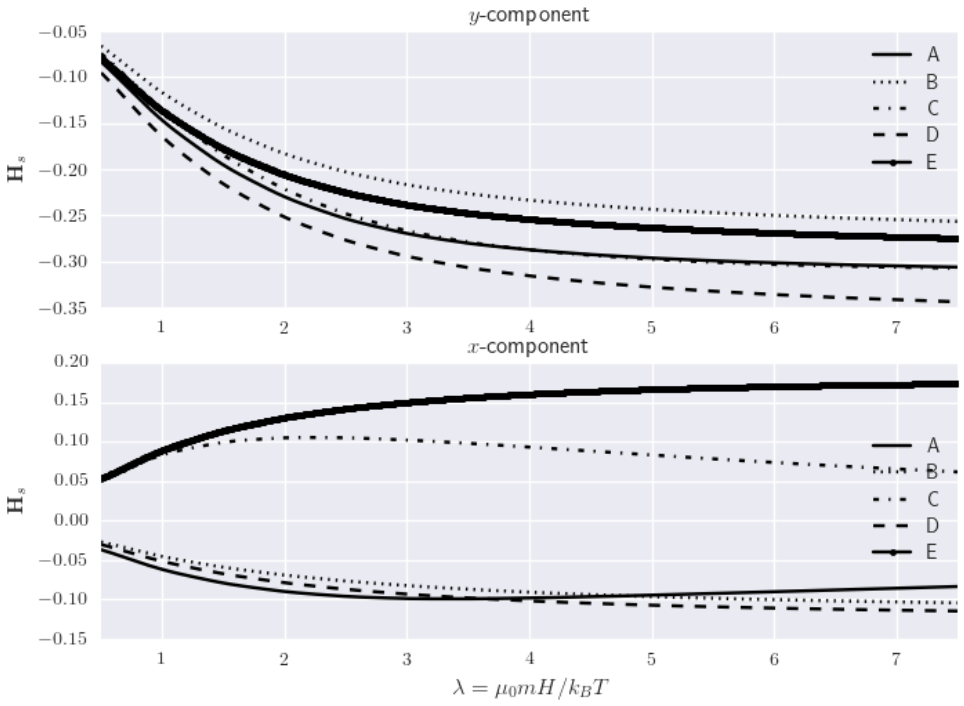

Figure 4.6: Plot of the (horizontal) x-component and (vertical) y-component of the stray field, say $\mathbf{H}_s \cdot \mathbf{e}_i$, versus the dimensionless magnetic parameter (the strength of the magnetic field relative to thermal energy due to Brownian motion), say λ, for the closure approximation. Here $\mathbf{e}_i$ denotes the standard Euclidean basis element in $\mathbb{R}^3$. Here $\mathbf{e}_1$ denotes the standard Euclidean basis element $(1, 0, 0) \in \mathbb{R}^3$. The important (fixed) numerical parameters are the Reynolds number $Re = 1$ and the Deborah number $De = 2$. Moreover, the labels A, B, C, and D, respectively, indicate the physical space locations for each vortices' center in Figure 4.2. More specifically, $A = (0.50390625, 0.50390625)$, $B = (0.27734375, 0.27734375)$, $C = (0.94140625, 0.27734375)$, and $D = (0.27734375, 0.94140625)$.

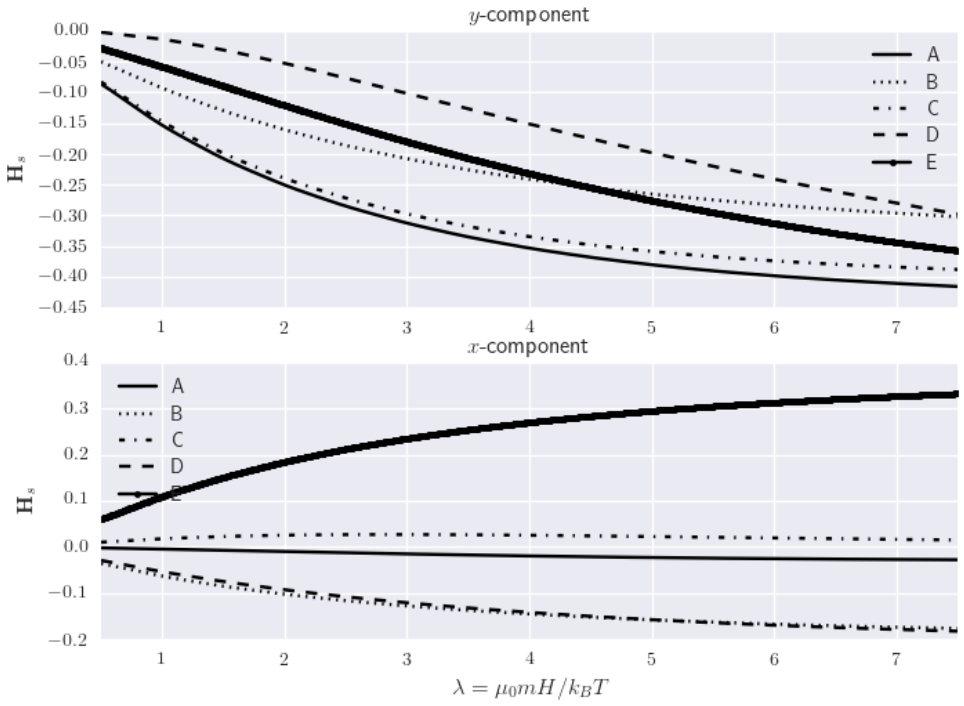

Figure 4.7: Plot of the (horizontal) x-component and (vertical) y-component of the stray field, say $\mathbf{H}_s \cdot \mathbf{e}_i$, versus the dimensionless magnetic parameter (the strength of the magnetic field relative to thermal energy due to Brownian motion), say λ, for the fully coupled system. Here $\mathbf{e}_i$ denotes the standard Euclidean basis element in $\mathbb{R}^3$. The important (fixed) numerical parameters are the Reynolds number $Re = 1$ and the Deborah number $De = 2$. Moreover, the labels A, B, C, and D, respectively, indicate the physical space locations where the vorticity exhibits sharp transitions from positive to negative values in Figure 4.2. More specifically, $A = (0.50390625, 0.50390625)$, $B = (0.12109375, 0.97265625)$, $C = (0.50390625, 0.90234375)$, and $D = (0.01953125, 0.86328125)$.

4.3 The magnetization

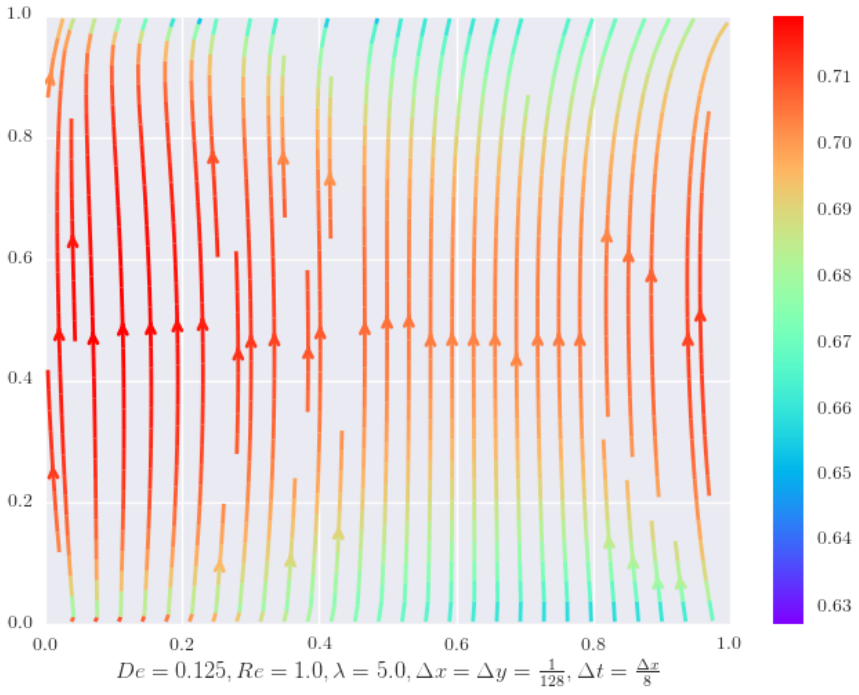

Figure 4.8: A streamplot, or streamline plot, of the (macroscopic) magnetization $\mathbf{M}$ as a two-dimensional vector field. The important numerical parameters are: the Deborah number $De = 0.125$, the Reynolds number $Re = 1$, and (the strength of the magnetic field relative to thermal energy due to Brownian motion) $\lambda = 5$. The vector field components are normalized so that (floating-point) data values from the interval $[0, 1]$ map to the RGBA color of corresponding colormap's luminance. The smallest intensity is violet and the largest is red, respectively[16].

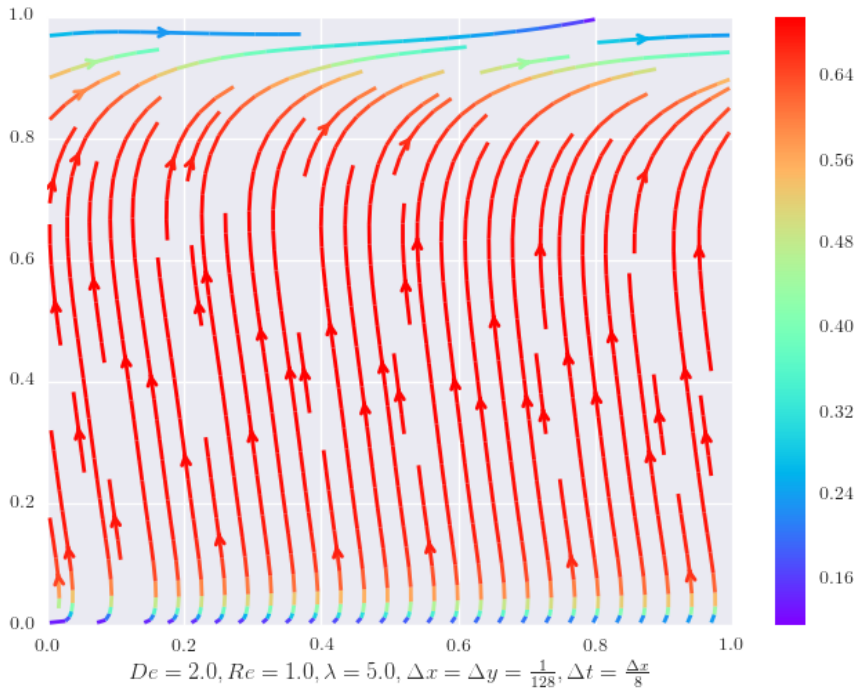

Figure 4.9: A streamplot, or streamline plot, of the (macroscopic) magnetization $\mathbf{M}$ as a two-dimensional vector field. The important numerical parameters are: the Deborah number $De = 0.125$, the Reynolds number $Re = 1$, and (the strength of the magnetic field relative to thermal energy due to Brownian motion) $\lambda = 5$. The vector field components are normalized so that (floating-point) data values from the interval $[0, 1]$ map to the RGBA color of corresponding colormap's luminance. The smallest intensity is violet and the largest is red, respectively[16].

In the case where $De < 1$, our magnetization instantly aligns itself with the external magnetic field $\mathbf{H}_{\text{ext}} = (0, 1, 0)$. Conversely, as we increase the Deborah number $De > 1$, the magnetization begins to align itself with the lid.

To investigate the spatial order of convergence, we compute the solution on three grids consecutively refined with a ratio of 2: 128×128, 256×256, and 512×512. For each simulation, we have a uniform time step $\Delta t = \dfrac{\Delta x}{8}$ with total time $t = 30$. The tolerance for convergence is set at 10^{-12}. The observed order of convergence in space using the solution on three consecutive grids in the L^2-norm is 1.8173636058.

4.4 Incremental viscosity

In a situation of shear flow, when a static external magnetic field is applied to a ferrofluid, thus impeding the (microscopic) magnetic particles' free rotation, we observe viscosity of the ferrofluid as a monotonic function of the magnetic field [41]. In fact, the viscosity reaches a saturation limit where the magnetic moments orient themselves along the applied magnetic field [40]. For the lid-driven cavity problem, the relationship is considerably different as the effective field is no longer uniform in physical space. In contrast, the micro-structure changes the (local) dynamics of the flow to such an extent that their magnetic stress and torque contributions to the effective viscosity of the ferrofluid may become negative. This phenomenon (for the

case of shear flow and an alternating magnetic field) was demonstrated experimentally in [26] and first coined as "negative change" in viscosity by Shliomis and Morozov [30].

In our quasi-three-dimensional model where we do not allow gradients in the z-direction, the magnetic stress, say σ_{xy}, is given by

$$\sigma_{xy} = \left(1 + \tfrac{5}{2}\Phi_0\right) \eta_0 \left(\kappa_{xy} + \kappa_{yx}\right) - \tfrac{1}{2} \left(H_x M_y - H_y M_x\right), \tag{4.4}$$

where $\kappa = \nabla \mathbf{v}$ denotes the gradient of the macroscopic velocity of the fluid, and $H_x, M_x (H_y, M_y)$ denote the horizontal x-direction (vertical y-direction) vector field components, respectively. The incremental viscosity, say $\Delta\eta$, is [41]:

$$\Delta\eta = \frac{\sigma_{xy}}{\kappa_{xy} + \kappa_{yx}} - \left(1 + \tfrac{5}{2}\Phi_0\right) \eta_0. \tag{4.5}$$

We calculate the incremental change of viscosity near the stream function's vortices and compare the results with our closure approximation. Indeed, we observe a "negative change" in viscosity.

Figure 4.10: A plot of the incremental viscosity, $\Delta\eta$, as a function of the dimensionless magnetic parameter (the strength of the magnetic field relative to thermal energy due to Brownian motion), $0.5 \leq \lambda \leq 7.5$. The important (fixed) numerical parameters are the Reynolds number, $Re = 1$ and the Deborah number, $De = 0.125$. Moreover, the labels A, B, C, D, and E, respectively, indicate the physical space locations where the vorticity exhibits sharp transitions from positive to negative values in Figure 4.2. More specifically, $A = (0.50390625, 0.50390625)$, $B = (0.12109375, 0.97265625)$, $C = (0.50390625, 0.90234375)$, $D = (0.01953125, 0.86328125)$. and $E = (0.03515625, 0.03515625)$.

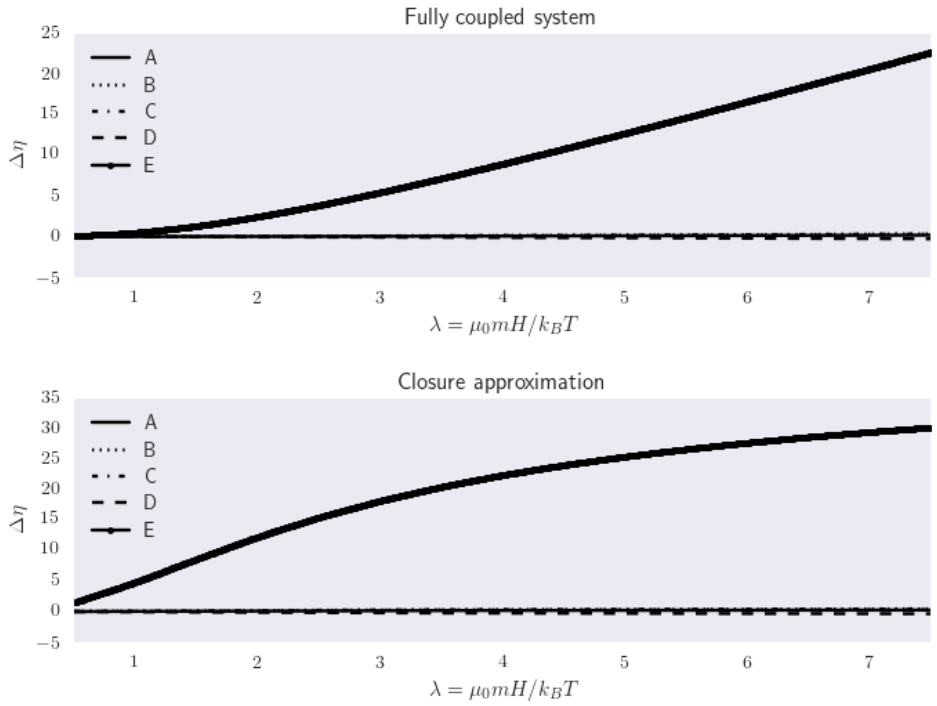

When De is small we have a monotonic relationship. That is, as we increase λ, thus hindering particle rotation, we get an (decrease) increase in viscosity near (away from) the externally applied magnetic field.

Figure 4.11: A plot of the incremental viscosity, $\Delta\eta$, as a function of the dimensionless magnetic parameter (the strength of the magnetic field relative to thermal energy due to Brownian motion), $0.5 \leq \lambda \leq 7.5$. The important (fixed) numerical parameters are the Reynolds number, $Re = 1$ and the Deborah number, $De = 2$. Moreover, the labels A, B, C, D, and E, respectively, indicate the physical space locations where the vorticity exhibits sharp transitions from positive to negative values in Figure 4.2. More specifically, $A = (0.50390625, 0.50390625)$, $B = (0.12109375, 0.97265625)$, $C = (0.50390625, 0.90234375)$, $D = (0.01953125, 0.86328125)$. and $E = (0.03515625, 0.03515625)$.

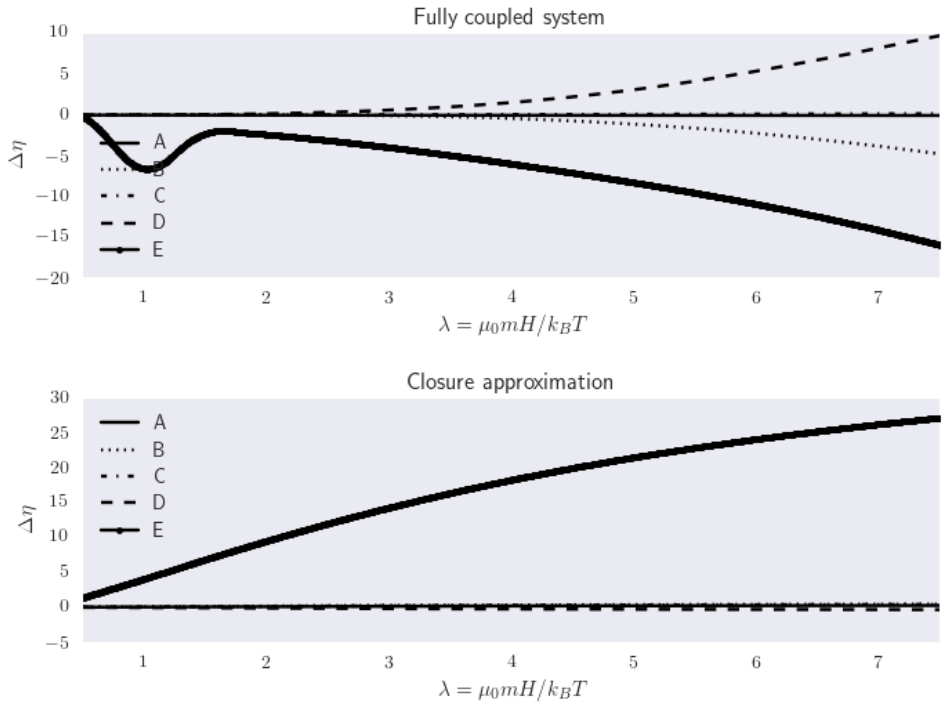

Our figures illustrate the dependence of the relative rotational viscosity on the Deborah number, $De \in \{0.125, 2.0\}$, over the dimensionless magnetic parameter (the strength of the magnetic field relative to thermal energy due to Brownian motion), $0.5 \leq \lambda \leq 7.5$. The plots demonstrate that the stronger the applied field, the steeper the decrease of $\Delta\eta$. As a matter of fact, the dependency $\Delta\eta(\lambda)$ is demonstrably non-monotonic.

When $De > 1$, increasing λ does not significantly deter free rotation; particle rotation is (locally) changing the flow dynamics and lowering the viscosity of the fluid by aligning themselves such that their rotation contributes to the flow.

By and large, this numerical experiment sheds light on the potential pitfalls of combining large De and moderate λ in closure approximation simulations. Our results demonstrate a poor quantitative agreement between the predictions of the closure approximation and a direct simulation in the case when the flow is no longer fixed and (local) angular velocity contributions are significant.

Results

Chapter 5

Conclusion

In this thesis, we developed a micro-macro approach for the modeling and computation of ferrofluids, wherein we solve every governing equation directly, that is, in both physical space (with two-dimensional spatial resolution) and configuration space (with complete three-dimensional resolution).

An incremental viscosity study for the lid-driven cavity problem with different dimensionless magnetic parameters (the strength of the magnetic field relative to thermal energy due to Brownian motion) observed "negative changes" in viscosity. As evident in figures 4.2 and 4.3, we have regions where the vorticity transitions from positive to negative values. While the (positive) vorticity in the main vortext acts to oppose the magnetic torque, and thus, positively increments the viscosity, the exact opposite occurs in the (negative) secondary vorticity regions. Moreover, our investigation re-

vealed that the (ad hoc) closure approximation by Shen and Doi is in relatively good agreement with the viscosity measurement of ferrofluids in the regime $De << 1$.

Admittedly, the most significant limitation of our quasi three-dimensional model was the simplifying assumption that there were no spatial gradients in the z-direction. Nonetheless, our investigation extends seamlessly to a three-dimensional flow at the cost of computation time. The dimensionality of the problem is formidable, and models with many configuration degrees of freedom are computationally intractable. This explains the relatively few studies in the literature where the Smoluchowski equation is solved directly. Our present study demonstrates that numerical simulation is indeed feasible. The numerical implementation is fully object-oriented in modern Fortran and the libraries are available on the software repository website bitbucket.

Appendix A

Recurrence relations

We aim to solve the dimensionless Smoluchowski equation

$$\frac{\partial \psi}{\partial t} + (\mathbf{v} \cdot \nabla_{\mathbf{x}})\, \psi = \frac{1}{De} \boldsymbol{\mathcal{R}} \cdot [\boldsymbol{\mathcal{R}} \psi + \lambda\, (\mathbf{h} \times \mathbf{u})\, \psi] - \boldsymbol{\mathcal{R}} \cdot (\boldsymbol{\Omega}\, \psi) \tag{A.1}$$

The probability density function $\psi(\theta, \phi)$ can be approximated up to machine precision by a truncated series of spherical harmonics, say $Y_n^m(\theta, \phi)$, which are the eigenfunctions of the Laplace-Beltrami operator $\boldsymbol{\mathcal{R}}^2 = \Delta_S$.

$$\psi(\mathbf{x}, \mathbf{u}(\theta, \phi), t) = \sum_{n=0}^{\infty} \sum_{m=-n}^{n} \psi_n^m Y_n^m(\theta, \phi). \tag{A.2}$$

In fact, the harmonics are a product of trigonometric functions, here represented as a complex exponential in ϕ, and (normalized) associate Legendre function in $\cos\theta$:

$$Y_n^m(\theta,\phi) = \bar{P}_n^m(\cos\theta)\exp(im\phi), \tag{A.3}$$

where

$$\bar{P}_n^m(\cos\theta) = \sqrt{\frac{(2n+1)}{2}\frac{(n-m)!}{(n+m)!}}P_n^m(\cos\theta), \tag{A.4}$$

where P_n^m are the associate Legendre functions satisfying Rodrigue's formula.

$$P_n^m(\cos\theta) = \frac{1}{2^n n!}\sin^m(\theta)\frac{d^{n+m}}{dx^{n+m}}\left(\cos^2(\theta)-1\right)^n. \tag{A.5}$$

Indeed, the (complex) harmonics possess unit power

$$\frac{1}{2\pi}\int_{\theta=0}^{\pi}\int_{\phi=0}^{2\pi} Y_n^m\left(Y_{n'}^{m'}\right)^* \sin\theta d\phi d\theta = \int_{S^2} Y_n^m\left(Y_{n'}^{m'}\right)^* dS = \delta_{nn'}\delta_{mm'}, \tag{A.6}$$

where * denotes the complex conjugate, and $\delta_{aa}=1$, $\delta_{ab}=0$ if $a\neq b$.

A.1 Real spherical harmonics

To this point the harmonics have been developed for complex functions. However, the solution to our Smoluchowski equation is real-valued and hence, we now develop

the real form of the spherical harmonics. These forms are about twice as efficient as the complex transforms and hence represent the preferred transforms of real functions.

We begin with the development of the synthesis of a real-valued function. Equation (A.2) can be written as

$$\psi = \sum_{n=0}^{\infty} \left(a_n^0 \overline{P}_n^0 + \sum_{m=1}^{n} \psi_n^{-m} Y_n^{-m} + \sum_{m=1}^{n} \psi_n^m Y_n^m \right). \tag{A.7}$$

Using the identity

$$P_n^{-m} = \begin{cases} (-1)^m \dfrac{(n-m)!}{(n+m)!} P_n^m, & \text{if} \quad |m| \leq n \\ 0, & \text{if} \quad |m| > n, \end{cases} \tag{A.8}$$

it follows that the above normalized (complex) spherical harmonic functions satisfy

$$Y_n^{m*} = (-1)^m Y_n^{-m}, \tag{A.9}$$

which in turn reveals that

$$\psi_n^{-m} = (-1)^m \psi_n^m. \tag{A.10}$$

Substituting these results into (A.7), we obtain

$$\psi = \sum_{n=0}^{\infty} \left[\psi_n^0 \overline{P}_n^0 + \sum_{m=1}^{n} 2\mathrm{Re}\left(\psi_n^m Y_n^m\right) \right]. \tag{A.11}$$

If we define

$$\psi_n^m = \tfrac{1}{2}\left(a_n^m - ib_n^m\right), \tag{A.12}$$

where $i = \sqrt{-1}$, denotes the imaginary unit, then the real form of the harmonic synthesis is

$$\psi(\theta,\phi) = \sum_{m=0}^{\infty}{}' \sum_{n=m}^{\infty} \overline{P}_n^m \left(a_n^m \cos(m\phi) + b_n^m \sin(m\phi)\right). \tag{A.13}$$

The prime notation on the first sum indicates that the first term corresponding to $m = 0$ is multiplied by $1/2$. The real form of the harmonic analysis can be obtained as

$$a_n^m = \frac{1}{2\pi}\int_{\theta=0}^{\pi}\int_{\phi=0}^{2\pi} \psi(\theta,\phi)\overline{P}_n^m \cos(m\phi)dS \tag{A.14}$$

and

$$b_n^m = \frac{1}{2\pi}\int_{\theta=0}^{\pi}\int_{\phi=0}^{2\pi} \psi(\theta,\phi)\overline{P}_n^m \sin(m\phi)dS \tag{A.15}$$

A.2 Complex analysis and synthesis

We utilize `modern_spherepack` [21], an object-oriented thread-safe modernization of NCAR's `SPHEREPACK3.2` [35], to validate our fully spectral implementation.

Since the library implements real harmonic analysis and synthesis, we supplied routines to transform gridded real-valued scalar arrays to the corresponding complex spectral coefficients. Furthermore, all of our routines use triangular truncation. The grid and spectral arrays must be rank 2 and rank 1, respectively; passing array sections is safe.

A.3 Complex index convention

The spectral data is assumed to be in a complex array of dimension

$$(M+1)(M+2)/2. \tag{A.16}$$

Here $M \leq NLAT - 1$ is the triangular truncation limit, where $NLAT$ denotes the number of gaussian grid points $0 \leq \theta \leq \pi$.

The coefficients are ordered so that first $(nm = 1)$ is $m = 0, n = 0$, second is $m = 0, n = 1$, $nm = M$ is $m = 0, n = M$, $nm = M + 1$ is $m = 1, n = 1$, etc.

$$
\begin{array}{ccccccc}
\psi_0^0 & \psi_1^0 & \psi_2^0 & \psi_3^0 & \cdots & \psi_M^0 \\
 & \psi_1^1 & \psi_2^1 & \psi_3^1 & \cdots & \psi_M^1 \\
 & & \psi_2^2 & \psi_3^2 & \cdots & \psi_M^2 \\
 & & & \psi_3^3 & \cdots & \psi_M^3 \\
 & & & & \ddots & \vdots
\end{array}
$$

A.4 Validating data structure implementation

We test our implementation with the functions

$$\psi(\theta, \phi) = \sin^2\theta \cos\theta \sin\phi \cos\phi \tag{A.17}$$

$$\widetilde{\psi}(\theta, \phi) = \exp(\psi), \tag{A.18}$$

and compare our results with the unit tests furnished by SPHEREPACK 3.2. The errors are all $\sim 10^{-16}$ for the moderate resolution of 15-many Gaussian (co)latitudinal points in θ and 18-many (uniform) Fourier longitudinal points in ϕ.

A.5 The angular momentum operator

In quantum mechanics, the (complex) spherical harmonics are understood in terms of the angular momentum operator

$$L = -i\boldsymbol{\mathcal{R}}, \tag{A.19}$$

where

$$L_x = i\sin\phi\frac{\partial}{\partial\theta} + i\cos\phi\cot\theta\frac{\partial}{\partial\phi}, \tag{A.20}$$

$$L_y = -i\cos\phi\frac{\partial}{\partial\theta} + i\sin\phi\cot\theta\frac{\partial}{\partial\phi}, \tag{A.21}$$

$$L_z = -i\frac{\partial}{\partial\phi} \tag{A.22}$$

for $L = L_x\,\mathbf{i} + L_y\,\mathbf{j} + L_z\,\mathbf{k}$.

A.5.1 Condon-Shortley phase

In the physics community it is common practive to include a phase factor of $(-1)^m$, commonly referred to as the Condon-Shortley phase, in the definition of the spherical harmonic functions. There is no mathematical requirement to use the Condon-Shortley phase, but including it simplifies the quantum mechanical operations, more specifically the application of raising and lowering operators.

Since SPHEREPACK 3.2 is geared toward the geodesy community who omit the Condon-Shortley phase factor, we must append our subroutines to include this factor. That is,

$$\widetilde{Y}_n^m(\theta,\phi) = (-1)^m \overline{P}_n^m(\cos\theta)\exp(im\phi), \tag{A.23}$$

we obtain that $L^2 = L_x^2 + L_y^2 + L_z^2 = -\mathcal{R}$ and

$$\mathcal{R}_x Y_n^m = \frac{1}{2} i \left(a_n^m (-1)^{m+1} Y_n^{m+1} + b_n^m (-1)^{m-1} Y_n^{m-1} \right) \tag{A.24}$$

$$\mathcal{R}_y Y_n^m = \frac{1}{2} \left(a_n^m (-1)^{m+1} Y_n^{m+1} - b_n^m (-1)^{m-1} Y_n^{m-1} \right) \tag{A.25}$$

$$\mathcal{R}_z Y_n^m = imY_n^m. \tag{A.26}$$

Validating $\mathcal{R}$ relations

Again, using the functions (A.17) and (A.18) we obtain errors $\sim 10^{-14}$ for (A.24), (A.25), and (A.26).

Appendix B

Derivation of spectral coefficients

B.1 The coefficients $A[\psi_n^m]$

Furthermore, from the identities of $\mathcal{R}$ acting on Y_n^m we now obtain that for

$$\mathbf{\Omega} = \Omega_x \, \mathbf{i} + \Omega_y \, \mathbf{j} + \Omega_z \, \mathbf{k} = \tfrac{1}{2} \nabla_x \times \mathbf{v}, \tag{B.1}$$

$$\mathcal{R}\cdot(\mathbf{\Omega}Y_n^m) = \frac{1}{2}i\left(a_n^m(-1)^{m+1}\Omega_x Y_n^{m+1} + b_n^m(-1)^{m-1}\Omega_x Y_n^{m-1}\right)$$
$$+\frac{1}{2}\left(a_n^m(-1)^{m+1}\Omega_y Y_n^{m+1} - b_n^m(-1)^{m-1}\Omega_y Y_n^{m-1}\right)$$
$$+ im\Omega_z Y_n^m, \tag{B.2}$$
$$= \frac{1}{2}i\left(a_n^m(-1)^{m+1}\Omega_x Y_n^{m+1} + b_n^m(-1)^{m-1}\Omega_x Y_n^{m-1}\right)$$
$$-i^2\frac{1}{2}\left(a_n^m(-1)^{m+1}\Omega_y Y_n^{m+1} - b_n^m(-1)^{m-1}\Omega_y Y_n^{m-1}\right)$$
$$+ im\Omega_z Y_n^m, \tag{B.3}$$
$$= \frac{1}{2}i\left(a_n^m(-1)^{m+1}\Omega_x Y_n^{m+1} + b_n^m(-1)^{m-1}\Omega_x Y_n^{m-1}\right)$$
$$+\frac{1}{2}i\left(a_n^m(-1)^{m+1}-i\Omega_y Y_n^{m+1} + b_n^m(-1)^{m-1}i\Omega_y Y_n^{m-1}\right)$$
$$+ im\Omega_z Y_n^m, \tag{B.4}$$
$$= \frac{1}{2}i\left(a_n^m\Omega^-(-1)^{m+1}Y_n^{m+1} + b_n^{m-1}\Omega^+(-1)^{m-1}Y_n^{m-1}\right) + i\Omega_z m Y_n^m, \tag{B.5}$$

where $\Omega^\pm = \Omega_x \pm i\Omega_y$. After integrating we find that

$$A[\psi_n^m] = \frac{1}{2}i\left(a_n^{m-1}\Omega^-(-1)^{m-1}\psi_n^{m-1} + b_n^{m+1}\Omega^+(-1)^{m+1}\psi_n^{m+1}\right) + i\Omega_z m\psi_n^m. \tag{B.6}$$

Using the functions (A.17), (A.18), and $\mathbf{\Omega} = (1, 2, 3)$ we obtain errors $\sim 10^{-13}$ for (B.6).

B.2 Recurrences for the spherical harmonics

Using the recurrence relations for the associate Legendre functions and including the $e^{im\phi}$ dependencies we arrive at

$$xY_n^m = \sqrt{\frac{(n-m+1)(n+m+1)}{(2n+1)(2n+3)}}Y_{n+1}^m + \sqrt{\frac{(n-m)(n+m)}{(2n-1)(2n+1)}}Y_{n-1}^m, \tag{B.7}$$

$$= \sqrt{\frac{((n+1)-m)((n+1)+m)}{(2(n+1)-1)(2(n+1)+1)}}Y_{n+1}^m + \sqrt{\frac{(n-m)(n+m)}{(2n-1)(2n+1)}}Y_{n-1}^m, \tag{B.8}$$

$$= h_{n+1}^m Y_{n+1}^m + h_n^m Y_{n-1}^m, \tag{B.9}$$

$$\sqrt{1-x^2}e^{i\phi}Y_n^{m-1} = \sqrt{\frac{(n+m)(n+m+1)}{(2n+1)(2n+3)}}Y_{n+1}^m - \sqrt{\frac{(n-m)(n-m+1)}{(2n-1)(2n+1)}}Y_{n-1}^m, \tag{B.10}$$

and

$$\sqrt{1-x^2}e^{-i\phi}Y_n^{m+1} = -\sqrt{\frac{(n-m)(n-m+1)}{(2n+1)(2n+3)}}Y_{n+1}^m + \sqrt{\frac{(n+m)(n+m+1)}{(2n-1)(2n+1)}}Y_{n-1}^m. \tag{B.11}$$

More specifically,

$$\sqrt{\frac{4\pi}{3}}Y_1^0 Y_n^m = xY_n^m, \tag{B.12}$$

$$= h_n^m Y_{n-1}^m + h_{n+1}^m Y_{n+1}^m, \tag{B.13}$$

$$\sqrt{\frac{8\pi}{3}}Y_1^1 Y_n^m = -\sqrt{1-x^2}e^{i\phi}Y_n^m, \tag{B.14}$$

$$= -\sqrt{\frac{(n+(m+1))(n+(m+1)+1)}{(2n+1)(2n+3)}}Y_{n+1}^{m+1}$$

$$+\sqrt{\frac{(n-(m+1))(n-(m+1)+1)}{(2n-1)(2n+1)}}Y_{n-1}^{m+1}, \tag{B.15}$$

$$= \sqrt{\frac{(n-m-1)(n-m)}{(2n-1)(2n+1)}}Y_{n-1}^{m+1} - \sqrt{\frac{(n+m+1)(n+m+2)}{(2n+1)(2n+3)}}Y_{n+1}^{m+1}, \tag{B.16}$$

$$= c_n^m Y_{n-1}^{m+1} - d_n^m Y_{n+1}^{m+1}, \tag{B.17}$$

for

$$c_n^m = \sqrt{\frac{(n-m-1)(n-m)}{(2n-1)(2n+1)}}, \tag{B.18}$$

$$d_n^m = \sqrt{\frac{(n+m+1)(n+m+2)}{(2n+1)(2n+3)}}. \tag{B.19}$$

Lastly,

$$\sqrt{\frac{8\pi}{3}}Y_1^{-1}Y_n^m = \sqrt{1-x^2}e^{-i\phi}Y_n^m, \tag{B.20}$$

$$= -\sqrt{\frac{(n-(m-1))(n-(m-1)+1)}{(2n+1)(2n+3)}}Y_{n+1}^{m-1}$$

$$+\sqrt{\frac{(n+(m-1))(n+(m-1)+1)}{(2n-1)(2n+1)}}Y_{n-1}^{m-1}, \tag{B.21}$$

$$= \sqrt{\frac{(n+m-1)(n+m)}{(2n-1)(2n+1)}}Y_{n-1}^{m-1} - \sqrt{\frac{(n-m+1)(n-m+2)}{(2n+1)(2n+3)}}Y_{n+1}^{m-1}, \tag{B.22}$$

$$= c_n^{-m}Y_{n-1}^{m-1} - d_n^{-m}Y_{n+1}^{m-1}. \tag{B.23}$$

B.3 The coefficients $P[\psi_n^m]$

By the chain rule, we see that

$$P[\psi_n^m] = \int_{S^2} \mathcal{R}\cdot[\psi(\mathbf{H}\times\mathbf{u})]\,(Y_n^m)^*\,dS, \tag{B.24}$$

$$= \int_{S^2} \mathcal{R}\cdot(\mathbf{H}\times\mathbf{u})\psi\,(Y_n^m)^*\,dS + \int_{S^2} \mathcal{R}\psi\cdot(\mathbf{H}\times\mathbf{u})\,(Y_n^m)^*\,dS. \tag{B.25}$$

After integrating by parts, we obtain:

$$\mathcal{R}\cdot(\mathbf{H}\times\mathbf{u})\,Y_n^m = 2\,(\mathbf{H}\cdot\mathbf{u})\,Y_n^m, \tag{B.26}$$

$$= \left(\sqrt{\frac{8\pi}{3}}\left(H^+Y_1^{-1} - H^-Y_1^1\right) + 2\sqrt{\frac{4\pi}{3}}H_zY_1^0\right)Y_n^m, \tag{B.27}$$

$$= H^+\left(\sqrt{\frac{8\pi}{3}}Y_1^{-1}Y_n^m\right) - H^{-1}\left(\sqrt{\frac{8\pi}{3}}Y_1^1Y_n^m\right)$$

$$+ 2H_z\left(\sqrt{\frac{4\pi}{3}}Y_1^0Y_n^m\right), \tag{B.28}$$

$$= H^+\left(c_n^{-m}Y_{n-1}^{m-1} - d_n^{-m}Y_{n+1}^{m-1}\right) - H^{-1}\left(c_n^mY_{n-1}^{m+1} - d_n^mY_{n+1}^{m+1}\right)$$

$$+ 2H_z\left(h_n^mY_{n-1}^m + h_{n+1}^mY_{n+1}^m\right). \tag{B.29}$$

That is,

$$\int_{S^2}\mathcal{R}\cdot(\mathbf{H}\times\mathbf{u})\psi\,(Y_n^m)^*\,dS = H^+\left(c_{n+1}^{-(m+1)}\psi_{n+1}^{m+1} - d_{n-1}^{-(m+1)}\psi_{n-1}^{m+1}\right)$$

$$- H^-\left(c_{n+1}^{m-1}\psi_{n+1}^{m-1} - d_{n-1}^{m-1}\psi_{n-1}^{m-1}\right)$$

$$+ 2H_z\left(h_{n+1}^m\psi_{n+1}^m + h_n^m\psi_{n-1}^m\right). \tag{B.30}$$

Putting $\mathbf{H} = (1, 2, 3)$ and using the functions (A.17), and (A.18), we obtain errors $\sim 10^{-16}$.

To evaluate

$$\int_{S^2}\mathcal{R}\psi\cdot(\mathbf{H}\times\mathbf{u})\,(Y_n^m)^*\,dS, \tag{B.31}$$

we use the `scalar triple product`

$$
\begin{aligned}
\mathcal{R}Y_n^m \cdot (\mathbf{H} \times \mathbf{u}) &= \mathbf{u} \cdot (\mathcal{R}Y_n^m \times \mathbf{H}) \\
&= \mathbf{u} \cdot (H_z \mathcal{R}_y Y_n^m - H_y \mathcal{R}_z Y_n^m, -H_z \mathcal{R}_x Y_n^m + H_x \mathcal{R}_z Y_n^m, H_y \mathcal{R}_x Y_n^m - H_x \mathcal{R}_y Y_n^m) \\
&= \frac{1}{2}\sqrt{\frac{8\pi}{3}}(Y_1^{-1} - Y_1^1)\,(H_z \mathcal{R}_y Y_n^m - H_y \mathcal{R}_z Y_n^m) \\
&+ i\frac{1}{2}\sqrt{\frac{8\pi}{3}}(Y_1^{-1} + Y_1^1)\,(-H_z \mathcal{R}_x Y_n^m + H_x \mathcal{R}_z Y_n^m) \\
&+ \sqrt{\frac{4\pi}{3}} Y_1^0\,(H_y \mathcal{R}_x Y_n^m - H_x \mathcal{R}_y Y_n^m) \\
&= \frac{1}{2}\sqrt{\frac{8\pi}{3}} Y_1^{-1}\,(H_z \mathcal{R}_y Y_n^m - H_y im Y_n^m - iH_z \mathcal{R}_x Y_n^m + iH_x im Y_n^m) \\
&+ \frac{1}{2}\sqrt{\frac{8\pi}{3}} Y_1^1\,(-H_z \mathcal{R}_y Y_n^m + H_y im Y_n^m - iH_z \mathcal{R}_x Y_n^m + iH_x im Y_n^m) \\
&+ \sqrt{\frac{4\pi}{3}} Y_1^0\,(H_y \mathcal{R}_x Y_n^m - H_x \mathcal{R}_y Y_n^m) \\
&= \frac{1}{2}\sqrt{\frac{8\pi}{3}} Y_1^{-1}\,(H_z\,(\mathcal{R}_y Y_n^m - i\mathcal{R}_x Y_n^m) - m\,(H_x + iH_y) Y_n^m) \\
&+ \frac{1}{2}\sqrt{\frac{8\pi}{3}} Y_1^1\,(-H_z\,(\mathcal{R}_y Y_n^m + i\mathcal{R}_x Y_n^m) - m(H_x - iH_y) Y_n^m) \\
&+ \sqrt{\frac{4\pi}{3}} Y_1^0\,(H_y \mathcal{R}_x Y_n^m - H_x \mathcal{R}_y Y_n^m) \\
&= \frac{1}{2}\sqrt{\frac{8\pi}{3}} Y_1^{-1}\left(H_z\,(\mathcal{R}_y Y_n^m - i\mathcal{R}_x Y_n^m) - mH^+ Y_n^m\right) \\
&+ \frac{1}{2}\sqrt{\frac{8\pi}{3}} Y_1^1\left(-H_z\,(\mathcal{R}_y Y_n^m + i\mathcal{R}_x Y_n^m) - mH^- Y_n^m\right) \\
&+ \sqrt{\frac{4\pi}{3}} Y_1^0\,(H_y \mathcal{R}_x Y_n^m - H_x \mathcal{R}_y Y_n^m)\,.
\end{aligned}
$$

For the first term we use the identity

$$\mathcal{R}_y Y_n^m - i\mathcal{R}_x Y_n^m = a_n^m (-1)^{m+1} Y_n^{m+1}, \tag{B.32}$$

along with (A.26) to obtain

$$\begin{aligned}
&\frac{1}{2}\sqrt{\frac{8\pi}{3}} Y_1^{-1} \left(H_z (\mathcal{R}_y Y_n^m - i\mathcal{R}_x Y_n^m) - mH^+ Y_n^m \right) \\
&= \frac{1}{2}\sqrt{\frac{8\pi}{3}} Y_1^{-1} \left(H_z a_n^m (-1)^{m+1} Y_n^{m+1} - mH^+ Y_n^m \right), \qquad \text{(B.33)} \\
&= \frac{1}{2} \left(H_z a_n^m (-1)^{m+1} \sqrt{\frac{8\pi}{3}} Y_1^{-1} Y_n^{m+1} \right. \\
&\left. - mH^+ \sqrt{\frac{8\pi}{3}} Y_1^{-1} Y_n^m \right), \qquad \text{(B.34)} \\
&= \frac{1}{2} H_z a_n^m (-1)^{m+1} \left(c_n^{-(m+1)} Y_{n-1}^m - d_n^{-(m+1)} Y_{n+1}^m \right) \\
&- \frac{1}{2} mH^+ \left(c_n^{-m} Y_{n-1}^{m-1} - d_n^{-m} Y_{n+1}^{m-1} \right). \qquad \text{(B.35)}
\end{aligned}$$

For the second term we employ the identity

$$\mathcal{R}_y Y_n^m + i\mathcal{R}_x Y_n^m = -b_n^m (-1)^{m-1} Y_n^{m-1}, \tag{B.36}$$

$$\frac{1}{2}\sqrt{\frac{8\pi}{3}}Y_1^1\left(-H_z(\mathcal{R}_y Y_n^m + i\mathcal{R}_x Y_n^m) - mH^- Y_n^m\right)$$

$$= \frac{1}{2}\sqrt{\frac{8\pi}{3}}Y_1^1\left(-H_z - b_n^m(-1)^{m-1}Y_n^{m-1} - mH^- Y_n^m\right), \tag{B.37}$$

$$= \frac{1}{2}\left(H_z b_n^m(-1)^{m-1}\sqrt{\frac{8\pi}{3}}Y_1^1 Y_n^{m-1}\right.$$

$$\left. -mH^-\sqrt{\frac{8\pi}{3}}Y_1^1 Y_n^m\right), \tag{B.38}$$

$$= \frac{1}{2}H_z b_n^m(-1)^{m-1}\left(c_n^{m-1}Y_{n-1}^m - d_n^{m-1}Y_{n+1}^m\right)$$

$$- \frac{1}{2}mH^-\left(c_n^m Y_{n-1}^{m+1} - d_n^m Y_{n+1}^{m+1}\right). \tag{B.39}$$

For the last term we use (A.24) and (A.25) to obtain

$$\sqrt{\frac{4\pi}{3}}Y_1^0\left(H_y\mathcal{R}_xY_n^m-H_x\mathcal{R}_yY_n^m\right)$$

$$=\sqrt{\frac{4\pi}{3}}Y_1^0\left(H_y\frac{1}{2}i\left(a_n^m(-1)^{m+1}Y_n^{m+1}+b_n^m(-1)^{m-1}Y_n^{m-1}\right)\right.$$

$$\left.-H_x\frac{1}{2}\left(a_n^m(-1)^{m+1}Y_n^{m+1}-b_n^m(-1)^{m-1}Y_n^{m-1}\right)\right), \tag{B.40}$$

$$=\frac{1}{2}\sqrt{\frac{4\pi}{3}}Y_1^0\left(iH_y\left(a_n^m(-1)^{m+1}Y_n^{m+1}+b_n^m(-1)^{m-1}Y_n^{m-1}\right)\right.$$

$$\left.-H_x\left(a_n^m(-1)^{m+1}Y_n^{m+1}-b_n^m(-1)^{m-1}Y_n^{m-1}\right)\right), \tag{B.41}$$

$$=\frac{1}{2}\sqrt{\frac{4\pi}{3}}Y_1^0\left((H_x+iH_y)b_n^m(-1)^{m-1}Y_n^{m-1}\right.$$

$$\left.+(-H_x+iH_y)a_n^m(-1)^{m+1}Y_n^{m+1}\right), \tag{B.42}$$

$$=\frac{1}{2}\sqrt{\frac{4\pi}{3}}Y_1^0\left(H^+b_n^m(-1)^{m-1}Y_n^{m-1}\right.$$

$$\left.-H^-a_n^m(-1)^{m+1}Y_n^{m+1}\right), \tag{B.43}$$

$$=\frac{1}{2}\left(H^+b_n^m(-1)^{m-1}\sqrt{\frac{4\pi}{3}}Y_1^0Y_n^{m-1}\right.$$

$$\left.-H^-a_n^m(-1)^{m+1}\sqrt{\frac{4\pi}{3}}Y_1^0Y_n^{m+1}\right), \tag{B.44}$$

$$=\frac{1}{2}\left(H^+b_n^m(-1)^{m-1}\left(h_n^{m-1}Y_{n-1}^{m-1}+h_{n+1}^{m-1}Y_{n+1}^{m-1}\right)\right.$$

$$\left.-H^-a_n^m(-1)^{m+1}\left(h_n^{m+1}Y_{n-1}^{m+1}+h_{n+1}^{m+1}Y_{n+1}^{m+1}\right)\right). \tag{B.45}$$

Putting all of this together we obtain

$$\begin{aligned}\mathcal{R}Y_n^m \cdot (\mathbf{H}\times\mathbf{u}) = &\frac{1}{2}H_z a_n^m(-1)^{m+1}\left(c_n^{-m}Y_{n-1}^{m-1} - d_n^{-m}Y_{n+1}^{m-1}\right) - \frac{1}{2}mH^+Y_n^m\\ &+\frac{1}{2}H_z b_n^m(-1)^{m-1}\left(c_n^{m}Y_{n-1}^{m+1} - d_n^{m}Y_{n+1}^{m+1}\right) - \frac{1}{2}mH^-Y_n^m\\ &+\frac{1}{2}\left(H^+b_n^m(-1)^{m-1}\left(h_n^{m-1}Y_{n-1}^{m-1} + h_{n+1}^{m-1}Y_{n+1}^{m-1}\right)\right.\\ &\left.-H^-a_n^m(-1)^{m+1}\left(h_n^{m+1}Y_{n-1}^{m+1} + h_{n+1}^{m+1}Y_{n+1}^{m+1}\right)\right). \end{aligned} \tag{B.46}$$

After integrating we find

$$\begin{aligned}&\int (Y_n^m)^*\mathcal{R}\psi\cdot(\mathbf{H}\times\mathbf{u})\,dS\\ &= \frac{1}{2}H_z\left(a_{n+1}^m(-1)^{m+1}c_{n+1}^{-(m+1)} + b_{n+1}^m(-1)^{m-1}c_{n+1}^{m-1}\right)\psi_{n+1}^m\\ &-\frac{1}{2}H_z\left(a_{n-1}^m(-1)^{m+1}d_{n-1}^{-(m+1)} + b_{n-1}^m(-1)^{m-1}d_{n-1}^{m-1}\right)\psi_{n-1}^m\\ &+\left((m+1)H^-c_{n+1}^{-(m+1)} - \frac{1}{2}H^+b_{n+1}^{m+1}(-1)^m h_{n+1}^m\right)\psi_{n+1}^{m+1}\\ &-\left((m+1)H^-d_{n-1}^{-(m+1)} + \frac{1}{2}H^+b_{n-1}^{m+1}(-1)^m h_n^m\right)\psi_{n-1}^{m+1}\\ &+\left((m-1)H^+c_{n+1}^{m-1} - \frac{1}{2}H^-a_{n+1}^{m-1}(-1)^m h_{n+1}^m\right)\psi_{n+1}^{m-1}\\ &-\left((m-1)H^+d_{n-1}^{m-1} + \frac{1}{2}H^-a_{n-1}^{m-1}(-1)^m h_n^m\right)\psi_{n-1}^{m-1}. \end{aligned} \tag{B.47}$$

Putting all of this together we obtain

$$
\begin{aligned}
&\int_{S^2} (Y_n^m)^* \mathcal{R} \cdot \left(\psi \left(\mathbf{H} \times \mathbf{u}\right)\right) \, dS \\
&= H^+ \left(c_{n+1}^{-(m+1)} \psi_{n+1}^{m+1} - d_{n-1}^{-(m+1)} \psi_{n-1}^{m+1} \right) \\
&- H^- \left(c_{n+1}^{m-1} \psi_{n+1}^{m-1} - d_{n-1}^{m-1} \psi_{n-1}^{m-1} \right) \\
&+ 2H_z \left(h_{n+1}^m \psi_{n+1}^m + h_n^m \psi_{n-1}^m \right) \\
&+ \frac{1}{2} H_z \left(a_{n+1}^m (-1)^{m+1} c_{n+1}^{-(m+1)} + b_{n+1}^m (-1)^{m-1} c_{n+1}^{m-1} \right) \psi_{n+1}^m \\
&- \frac{1}{2} H_z \left(a_{n-1}^m (-1)^{m+1} d_{n-1}^{-(m+1)} + b_{n-1}^m (-1)^{m-1} d_{n-1}^{m-1} \right) \psi_{n-1}^m \\
&+ \left((m+1) H^- c_{n+1}^{-(m+1)} - \frac{1}{2} H^+ b_{n+1}^{m+1} (-1)^m h_{n+1}^m \right) \psi_{n+1}^{m+1} \\
&- \left((m+1) H^- d_{n-1}^{-(m+1)} + \frac{1}{2} H^+ b_{n-1}^{m+1} (-1)^m h_n^m \right) \psi_{n-1}^{m+1} \\
&+ \left((m-1) H^+ c_{n+1}^{m-1} - \frac{1}{2} H^- a_{n+1}^{m-1} (-1)^m h_{n+1}^m \right) \psi_{n+1}^{m-1} \\
&- \left((m-1) H^+ d_{n-1}^{m-1} + \frac{1}{2} H^- a_{n-1}^{m-1} (-1)^m h_n^m \right) \psi_{n-1}^{m-1}. \qquad \text{(B.48)}
\end{aligned}
$$

To conclude,

$$
\begin{aligned}
P[\psi_n^m] = & \frac{1}{2} H_z \left(a_{n+1}^m (-1)^{m+1} c_{n+1}^{-(m+1)} + b_{n+1}^m (-1)^{m-1} c_{n+1}^{m-1} + 2h_{n+1}^m \right) \psi_{n+1}^m \\
& - \frac{1}{2} H_z \left(a_{n-1}^m (-1)^{m+1} d_{n-1}^{-(m+1)} + b_{n-1}^m (-1)^{m-1} d_{n-1}^{m-1} + 2h_n^m \right) \psi_{n-1}^m \\
& + \left(H^- \left[(m+1) c_{n+1}^{-(m+1)} + d_{n-1}^{m-1} \right] - \frac{1}{2} H^+ b_{n+1}^{m+1} (-1)^m h_{n+1}^m \right) \psi_{n+1}^{m+1} \\
& - \left(H^- \left((m+1) d_{n-1}^{-(m+1)} - c_{n+1}^{m-1} \right) + \frac{1}{2} H^+ b_{n-1}^{m+1} (-1)^m h_n^m \right) \psi_{n-1}^{m+1} \\
& + \left(H^+ \left[(m-1) c_{n+1}^{m-1} - d_{n-1}^{-(m+1)} \right] - \frac{1}{2} H^- a_{n+1}^{m-1} (-1)^m h_{n+1}^m \right) \psi_{n+1}^{m-1} \\
& - \left(H^+ \left[(m-1) d_{n-1}^{m-1} + c_{n+1}^{-(m+1)} \right] + \frac{1}{2} H^- a_{n-1}^{m-1} (-1)^m h_n^m \right) \psi_{n-1}^{m-1}. \qquad \text{(B.49)}
\end{aligned}
$$

Bibliography

[1] A. Harten, B. Engquist, S. Osher and S. R. Chakravarthy. Uniformly High Order Accurate Essentially Non-oscillatory Schemes, {III}. *Journal of Computational Physics*, 131(1):3 – 47, 1997.

[2] A.J. Chorin. Numerical solution of the Navier-Stokes equations. *Math. Comput.*, 22:745–762, 1968.

[3] J. P. Boyd. *Chebyshev and Fourier spectral methods*. Dover Publications, 2001.

[4] C. J. García-Cervera. Numerical micromagnetics: a review. *Bol. Soc. Esp. Mat. Apl.*, 39:103–135, 2007.

[5] C. J. García-Cervera and A. M. Roma. Adaptive mesh refinement for micromagnetics simulations. *IEEE transactions on magnetics*, 42(6):1648–1654, 2006.

[6] S. Elborai H. Xiaowei C. Rinaldi, A. Chaves and M. Zahn. Magnetic fluid rheology and flows. *Current Opinion in Colloid & Interface Science*, 10(3-4):141 – 157,

2005.

[7] C. Shu and S. Osher. Efficient implementation of essentially non-oscillatory shock-capturing schemes, II. pages 328–374, 1989.

[8] A.J. Chorin and J.E. Marsden. *A Mathematical Introduction to Fluid Mechanics*, volume 4 of *Texts in Applied Mathematics*. Springer, third edition, 2000.

[9] R. Courant, K. Friedrichs, and H. Lewy. On the partial difference equations of mathematical physics. *IBM journal*, 11(2):215–234, 1967.

[10] D. L. Brown, R. Cortez, M. L. and Minion. Accurate projection methods for the incompressible Navier–Stokes equations. *Journal of computational physics*, 168(2):464–499, 2001.

[11] D. R. Fredkin and T. R. Koehler. Hybrid method for computing demagnetizing fields. *IEEE Transactions on Magnetics*, 26(2):415–417, Mar 1990.

[12] D. R. Durran. *Numerical methods for wave equations in geophysical fluid dynamics*, volume 32. Springer Science & Business Media, 2013.

[13] E. Erturk, T.C. Corke, and C. Gökçöl. Numerical solutions of 2-D steady incompressible driven cavity flow at high Reynolds numbers. *International Journal for Numerical Methods in Fluids*, 48(7):747–774, 2005.

[14] G. Folland. *Introduction to partial differential equations*. Princeton university press, 1995.

[15] F. H. Harlow and J. E. Welch. Numerical calculation of time-dependent viscous incompressible flow of fluid with free surface. *Physics of Fluids (1958-1988)*, 8(12):2182–2189, 1965.

[16] J. D. Hunter. Matplotlib: A 2d graphics environment. *Computing In Science & Engineering*, 9(3):90–95, 2007.

[17] P. N. Swarztrauber J. Adams and R. Sweet. FISHPACK - Efficient FORTRAN Subprograms for the Solution of Separable Elliptic Partial Differential Equations. National Center for Atmospheric Research. `https://www2.cisl.ucar.edu/resources/legacy/fishpack`, 1999.

[18] P. Colella J. B. Bell and M. G. Harland. A second-order projection method for the incompressible navier-stokes equations. *Journal of Computational Physics*, 85(2):257 – 283, 1989.

[19] J. D. Jackson. *Classical Electrodynamics*. Wiley, third edition, 1998.

[20] J. Kim and P. Moin. Application of a fractional-step method to incompressible navier-stokes equations. *Journal of Computational Physics*, 59(2):308 – 323, 1985.

[21] J. T. Lo Kim Lin. modern_spherepack. https://github.com/jlokimlin/modern_spherepack.git, 2015.

[22] J. T. Lo Kim Lin. closure_approximator. https://zellerback@bitbucket.org/zellerback/closure_approximator.git, 2016.

[23] J. T. Lo Kim Lin. maxwell_solver. https://zellerback@bitbucket.org/zellerback/maxwell_solver.git, 2016.

[24] J. T. Lo Kim Lin. modern_fishpack. https://github.com/jlokimlin/modern_fishpack.git, 2016.

[25] J. T. Lo Kim Lin. navier_stokes_solver. https://zellerback@bitbucket.org/zellerback/navier_stokes_solver.git, 2016.

[26] M. I. Shliomis J.C. Bacri, R. Perzynski and G. I. Burde. "negative-viscosity" effect in a magnetic fluid. *Phys. Rev. Lett.*, 75:2128–2131, Sep 1995.

[27] L. R. Philip. Discrete models for the numerical analysis of time-dependent multidimensional gas dynamics. *Journal of Computational Physics*, 63(2):458 – 476, 1986.

[28] M. Doi. Molecular dynamics and rheological properties of concentrated solutions of rodlike polymers in isotropic and liquid crystalline phases. *Journal of Polymer Science: Polymer Physics Edition*, 19(2):229–243, 1981.

[29] M. Doi and S. F. Edwards. *The Theory of Polymer Dynamics*. Oxford University Press, 1986.

[30] M. I. Shliomis and M. I. Konstantin. Negative viscosity of ferrofluid under alternating magnetic field. *Physics of Fluids (1994-present)*, 6(8):2855–2861, 1994.

[31] M. Metcalf. The seven ages of Fortran. *Journal of Computer Science & Technology (ISSN 1666-6038)*, 11(1):1–8, 2011.

[32] E. Merzbacher. *Quantum Mechanics*. Wiley, 1977.

[33] O. Reynolds. An Experimental Investigation of the Circumstances Which Determine Whether the Motion of Water Shall Be Direct or Sinuous, and of the Law of Resistance in Parallel Channels. *Philosophical Transactions of the Royal Society of London*, 174:pp. 935–982, 1883.

[34] P. N. Swarztrauber. A direct Method for the Discrete Solution of Separable Elliptic Equations. *SIAM Journal on Numerical Analysis*, 11(6):1136–1150, 1974.

[35] P. N. Swarztrauber. On Computing the Points and Weights for Gauss–Legendre Quadrature. *SIAM Journal on Scientific Computing*, 24(3):945–954, 2003.

[36] R. Courant and K. Friedrichs and H. Lewy. On the Partial Difference Equations of Mathematical Physics. *IBM Journal of Research and Development*, 11(2):215–234, March 1967.

[37] R. G. Larson and H. C. Ottinger. Effect of molecular elasticity on out-of-plane orientations in shearing flows of liquid-crystalline polymers. *Macromolecules*, 24(23):6270–6282, 1991.

[38] R. Keunings. Micro-macro methods for the multiscale simulation of viscoelastic flow using molecular models of kinetic theory. *Rheology reviews*, pages 67–98, 2004.

[39] R. E. Rosensweig. *Ferrohydrodynamics*. Cambridge University Press, New York, NY, 1985.

[40] S. Odenbach and S. Thurm. *Magnetoviscous Effects in Ferrofluids*. Springer Berlin Heidelberg, Berlin, Heidelberg, 2002.

[41] J. P. Shen and M. Doi. Effective viscosity of magnetic fluids. *Journal of the Physical Society of Japan*, 59(1):111–117, 1990.

[42] C. Shu and S. Osher. Efficient Implementation of Essentially Non-oscillatory Shock-capturing Schemes, II. *J. Comput. Phys.*, 83(1):32–78, July 1989.

[43] W. A. Strauss. *Partial differential equations*, volume 92. Wiley New York, 1992.

[44] K.N. Ghia U. Ghia and C.T. Shin. High-re solutions for incompressible flow using the navier-stokes equations and a multigrid method. *Journal of Computational Physics*, 48(3):387 – 411, 1982.

[45] V. Faraoni, and M. Grosso, and S. Crescitelli, P. Maffettone. The rigid-rod model for nematic polymers: an analysis of the shear flow problem. *Journal of Rheology (1978-present)*, 43(3):829–843, 1999.

[46] W. Rudin. *Real and Complex Analysis*. McGraw-Hill Science/Engineering/Math, third edition, 1986.

[47] E. W. Weisstein. Infinitesimal rotation. From MathWorld–A Wolfram Web Resource. `http://mathworld.wolfram.com/InfinitesimalRotation.html`, 2014. [Online; accessed September-25-2014].

[48] L. B. Zhang. A second-order upwinding finite difference scheme for the steady Navier-Stokes equations in primitive variables in a driven cavity with a multigrid solver. *ESAIM: Mathematical Modeling and Numerical Analysis - Modèlisation Mathèmatique et Analyse Numèrique*, 24(1):133–150, 1990.